CENTRIFUGAL COMPRESSOR MODELING DEVELOPMENT AND VALIDATION FOR A TURBOCHARGER COMPONENT MATCHING SYSTEM

by

CHRISTOPHER ERIK ERICKSON

B.S., Kansas State University, 2006

A THESIS

submitted in partial fulfillment of the requirements for the degree

MASTER OF SCIENCE

Department of Mechanical and Nuclear Engineering
College of Engineering

KANSAS STATE UNIVERSITY
Manhattan, Kansas

2008

Approved by:

Major Professor
Kirby S. Chapman, Ph.D.

Copyright

Abstract

This thesis outlines the development of a centrifugal compressor model for the Turbocharger Component Matching System (TuCMS) software package that can be used to inexpensively analyze turbocharger performance. The TuCMS can also be used to match turbocharger components to integrate and optimize turbocharger-engine performance. The software system is being developed with the intent to reduce the time taken to experimentally match a turbocharger with an engine, a task that is key to engine emission reductions. The TuCMS uses one-dimensional thermo-fluid equations to analyze the compressor side of a turbocharger. For each compressor component, the program calculates the velocities, pressures, temperatures, pressure losses, work consumption, and efficiencies for a specified set of turbocharger geometry, atmospheric conditions, rotational speed, and fluid mass flow rate. The compressor includes established loss models found in the open literature. The TuCMS utilizes a component-based architecture to simplify model enhancements. The TuCMS can be used as a cost effective engineering tool for preliminary turbocharger testing during engine upgrades and modifications. In this thesis, the TuCMS compressor model was used as an analysis tool to further understand the Variable Geometry Turbocharger (VGT) experimental results. The VGT is a unique turbocharger that can change the diffuser vane angle over a wide range of positions. The change in diffuser vane angle results in optimal turbocharger performance at various operating conditions, and potentially increases the operating range. The purpose for the use of the TuCMS compressor model analysis is to identify the change in performance as the diffuser vane angles are adjusted. The TuCMS can ideally be used as a control program for the VGT to adjust the diffuser vane angles as the compressor load changes and insure the compressor is operating at the highest efficiency.

Table of Contents

List of Figures

List of Tables

Acronyms

NGML	National Gas Machinery Laboratory
PRCI	Pipeline Research Council International, Inc.
TuCMS	Turbocharger Component Matching System
VGT	Variable Geometry Turbocharger

Nomenclature

A	Area
a	Velocity of sound
B	Fractional area blockage
C	Absolute velocity
c	Blade chord
c_p	Specific heat at constant pressure
h	Enthalpy
I	Work input coefficient
I_b	Impeller blade work input coefficient
L	Mean streamline meridional length
L_B	Blade mean camberline length
M	Mach number
$\dot{m}$	Mass flow rate
N	Rotational speed of turbocharger
p	Pressure
R	Rothalpy
r	Radius
R_g	Gas constant for air
Re_d	Reynolds number based on pipe diameter
Re_e	Reynolds number based on surface roughness
s	Clearance gap width
T	Temperature
t_b	Blade thickness

U	Blade speed
V	Velocity
W	Relative velocity
w	Passage width
$\overline{x}$	Average (bar over variable represents average)
Z	Number of blades

Greek Variables

α	Flow angle – actual
β	Flow angle – relative
δ	Deviation angle
ε	Impeller meanline radius ratio
ϕ	Flow coefficient
γ	Ratio of specific heats
η	Efficiency
κ_m	Streamline curvature
λ	Distortion factor
μ	Gas viscosity
θ	Compressor blade angle
ρ	Density
σ	Slip factor
$\bar{\omega}$	Non-dimensional pressure loss

Scripts

Subscripts	
corr	Corrected
id	Ideal
in	Inlet
m	Meridional coordinate direction
out	Discharge or outlet of system
r	Relative
s	Static
stoich	Stoichiometric
t	Total
Th	Throat parameter
U	Tangential coordinate direction
Superscripts	
*	Sonic flow conditions

Acknowledgements

This thesis would not have been possible without the people that supported and encouraged me. I want to thank my adviser Dr. Kirby Chapman, the director of the National Gas Machinery Laboratory (NGML). He gave me the opportunity to work on this research and introduced me to the natural gas energy and transmission industry. He also provided guidance and took time to discuss my research and lend his knowledge when issues arose. I want to thank Dr. Ali Keshavarz for his help and insight. I want to thank Jeet Sengupta, a Ph.D. student at the NGML, who has been my guide in debugging the compressor modeling programming code and whom developed the turbine model for the Turbocharger Component Matching System (TuCMS). I also want to thank the rest of my colleagues at the NGML for making it a great place to work. I want to thank Dr. Donald L. Fenton and Dr. Terry Beck for being members of my defense committee. I want to thank the Compressor and Pump Station Technical Committee of Pipeline Research Council International (PRCI) for funding the development of the TuCMS program and for their guidance and encouragement during the development of the engineering models. Finally, I want to thank my parents and sisters for encouraging me to go further with my education and teaching me the things to be a good person and hard worker.

CHAPTER 1 - Introduction

The focus of this thesis has been the development of the centrifugal compressor model for a turbocharger component matching system. The following objectives are the focus of the model development and this thesis:

- Develop a compressor model that applies first engineering principles to calculate individual component performance based on a set of measurable parameters; and
- Validate the model using experimental data collected at the National Gas Machinery Laboratory for a selected turbocharger compressor.

Companies with large legacy reciprocating engines need cost-effective options to meet the impending oxides of nitrogen (NO_x) emissions requirement of 0.5 g/bhp-hr (PRCI. 2005). These options should neither increase other pollutants nor have a detrimental effect on the engine performance and reliability. An option to these requirements is turbocharging the engine to create precise trapped equivalence ratios. Providing a precise lean trapped equivalence ratio lowers the combustion temperature and thus the production rate of NO_x. Consequently, the quantity of air mass trapped in the cylinder directly corresponds to NO_x emissions. Figure 1.1 shows a representation of how the emissions nitrogen oxides (NO_x), carbon monoxide (CO), and unburned hydrocarbons (HC) react to the lean fuel to air equivalence ratio.

A potential problem in turbocharging the engine to precise lean trapped equivalence ratios is developing a precision designed turbocharger and a precise turbocharger-engine match. Current practices include rule-of-thumb or prior experience to design turbochargers and develop the engine-turbocharger match. Such techniques may have been appropriate when emissions limits were high, but they are not sufficient in today's world of more stringent emissions limits. In the natural gas transmission industry, precisely matching turbochargers to engines is further problematic because most engines are unique – they have been modified over the last several decades in numerous ways.

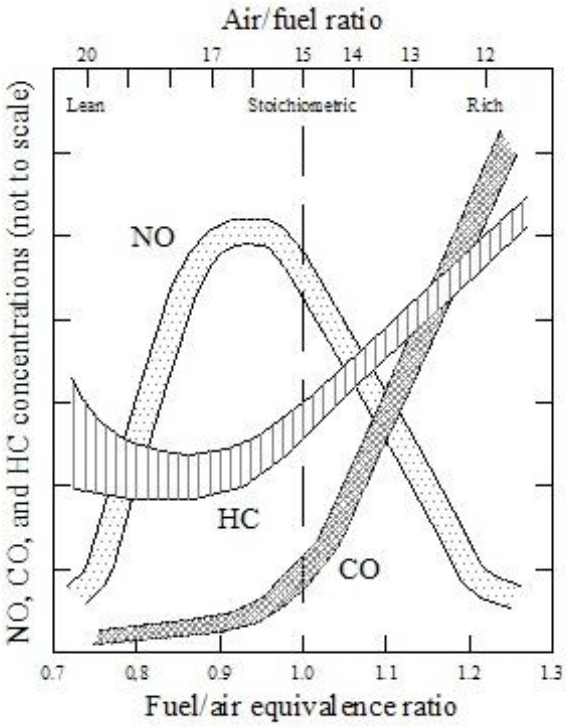

Figure 1.1 Variation of emissions concentration to fuel to air equivalence ratio (Heywood. 1988)

The matching problem can be more easily assessed if engineers have a computer based tool that will ensure correct turbocharger-engine matching. Such a tool should have the following outcomes:

- An engine model;
- A turbocharger model;
- A fundamental physics-based turbocharger-engine matching algorithm; and
- Algorithms to optimize the system.

As described by Baines (2005) "the turbocharger is a turbine-driven compressor," and because a turbocharger model is one of the goals of the matching system, a robust turbocharger model must include both a compressor model and a turbine model along with an algorithm that accurately matches the two components. Accurately matched turbocharger components maximize overall turbocharger efficiency to ensure a precise amount of air is delivered to the engine to produce lower NO_x emissions without reducing engine efficiency.

A search of the open literature has shown that a complete model of a turbocharger matching system is not in public existence, and, because this is the case, the development of a matching system is desired. To develop this turbocharger matching system as mentioned earlier, a compressor model and turbine model need to be developed independently and coupled. This thesis describes the compressor modeling process and validation.

The turbocharger selected to validate the compressor model is a prototype that is unique in that it utilizes varying diffuser vane positions. Researchers at the National Gas Machinery Laboratory collected an abundance of data for the prototype that has been labeled the Variable Geometry Turbocharger (VGT) (Chapman, et al. 2007). Because this unique turbocharger has a wide range of vane positions, the vane angle that results in the optimal turbocharger performance at various operating conditions is unknown. Another objective of this thesis is to estimate the physical characteristics and performance of the different internal components of the turbocharger for varying operating conditions, such as speed and ambient temperature.

The rest of this thesis describes the tasks undertaken to produce the compressor model for the turbocharger component and engine matching system. A literature review of information for a turbocharger compressor and turbine, the energy destruction losses produced by a centrifugal compressor, and an overview of the VGT are reviewed in Chapter 2. Chapter 3 mathematically describes the physical characteristics for the compressor as fluid flows through each component. Chapter 4 describes the solution method used to calculate the mathematical descriptions given in Chapter 3. Chapter 5 describes the validation of the model with the VGT and also describes the results of the for a VGT loss analysis. Chapter 6 provides the conclusions and future work for the research represented in this thesis.

CHAPTER 2 - Literature review

This section describes the literature on the subjects of turbochargers, centrifugal compressors, radial and axial turbines, potential energy destruction losses in the centrifugal compressor, and an overview of the Variable Geometry Turbocharger concept and prototype.

Turbocharger

Watson and Janota (1982) provide one of the more comprehensive treatises on turbochargers. They describe a turbocharger as a turbine driven compressor that is used to increase the air flow rate into an internal combustion engine. This is accomplished by using the compressor to compress air and increase the air flow into the cylinders of the internal combustion engine. The compressor is driven by a turbine that extracts energy from the exhaust gases of the internal combustion engine and then converts that energy to shaft power. The arrangement is ideal because the compressor is not using power from the engine drive shaft or any other external power source. Turbochargers are efficient in that the turbine utilizes the exhaust gas energy that is typically rejected to the atmosphere in the case of a naturally aspirated engine. For the turbocharger to operate efficiently, the mass flow rate of exhaust gases passing through the turbine must equal the sum of the compressor air mass flow rate and the fuel mass flow rate added. An exhaust waste gate can be used to avoid over-speeding the turbocharger when compensating for high cylinder pressures of a turbocharger operating over a wide speed and load range (Waston and Janota. 1982). The exhaust waste gate's purpose is to bypass the excess engine exhaust gas past the turbine to ensure an energy balance between the compressor, engine, and turbine. The energy balance of the power produced by the turbine must be equal or be slightly greater than the power consumed by the compressor and bearing losses.

Configurations

There are many types and configurations of turbochargers. Figure 2.1 and Figure 2.2 show different types turbochargers. Watson and Janota (1982), Heywood (1988), Aungier (2000), Baines (2005), Boyce (2003), and others describe the key components that make up a turbocharger as: compressor, turbine linked to the compressor by a shaft, bearings to support the shaft, shaft seals to separate the exhaust and the air, water cooling jacket, and oil system. Commercially the compressor is typically a centrifugal machine because an axial machine is expensive and requires several stages of rotor and stator combinations to accomplish the necessary pressure ratio a centrifugal machine can produce in a single stage (Watson and Janota. 1982). The turbine is either an axial or radial machine. The two most common turbocharger configurations are (1) a centrifugal compressor and a radial turbine, or (2) a centrifugal compressor and an axial turbine. Figure 2.1 and Figure 2.2 show examples of the two common turbocharger configurations. The figures are good representations of the two common configurations and show the cut-away views of the main components for each turbocharger.

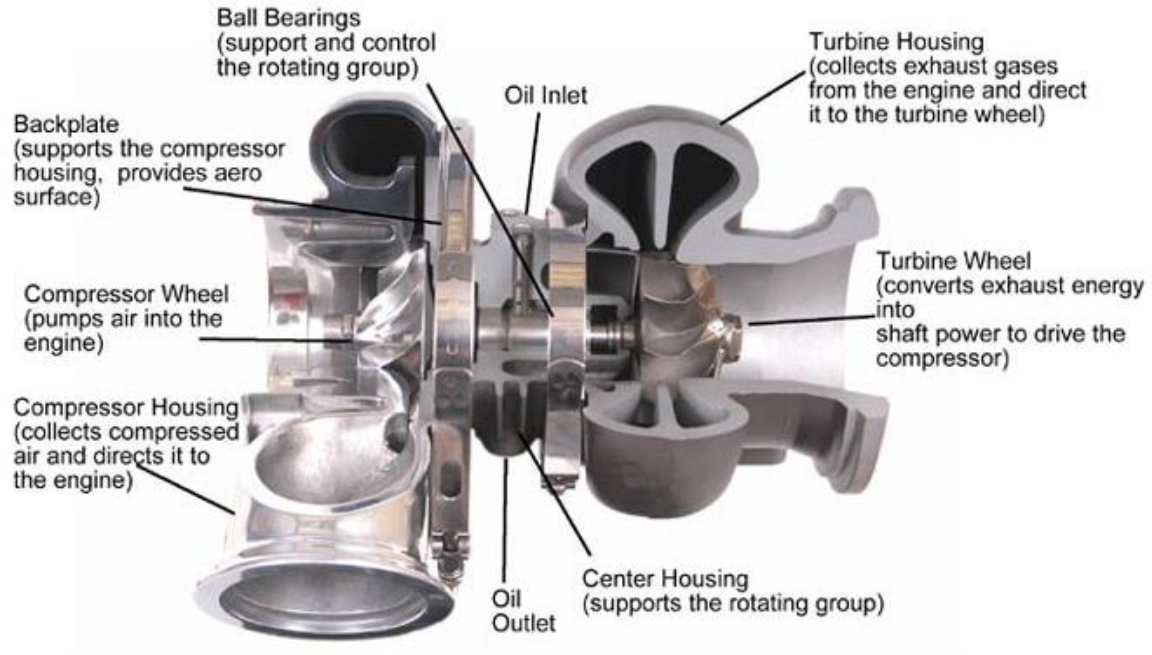

Figure 2.1 Cut-away view of centrifugal compressor and radial turbine turbocharger (Engine Logics Inc.)

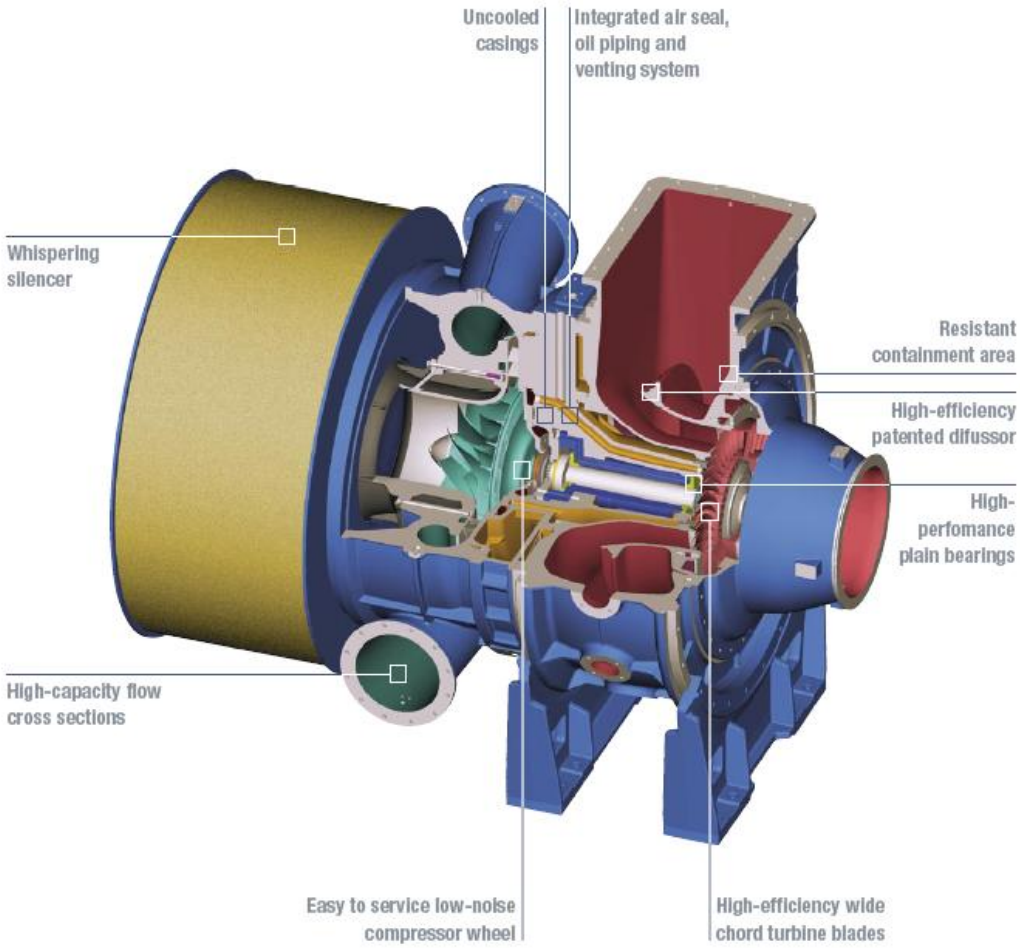

Figure 2.2 Cut-away view of centrifugal compressor and axial turbine turbocharger (MAN B&W. 2008)

Components

Turbochargers can be separated into three sections: compressor, turbine, and sealed compartment. These sections are composed of many additional components.

Compressor

Figure 2.3 shows the primary components of a centrifugal compressor: impeller, diffuser, and volute. Boyce (2003) describes the impeller as the rotating component of the centrifugal compressor configured from two components. The first component of the impeller is the inducer that acts as an axial rotor and draws the fluid flow into the impeller in the axial direction. The second component of the impeller is the set of radial

blades that energize the fluid and impart mechanical energy to the fluid to increase the fluid total enthalpy and total pressure. Fluid flow enters the impeller in the axial direction and departs energized and in the radial direction. The two types of impellers encountered in the natural gas transmission industry are the open faced and closed faced impellers. Testing experience at the NGML clearly suggests that the most current turbocharger compressors utilize open faced impellers.

The diffuser is the non-rotating component of the compressor that converts a portion of the kinetic energy in the flowing fluid to pressure energy (Boyce. 2003). The kinetic energy conversion is accomplished by using a vaneless and a vaned diffuser in series. The vaneless portion is the first stage of the diffuser and its main purpose is to reduce the Mach number by reducing the velocity of the fluid flow leaving the impeller from possible supersonic conditions to subsonic conditions (Boyce. 2003). The vaned portion is the second stage of the diffuser.

The volute collects the fluid exiting the diffuser and routes it to a discharge pipe. Volutes typically have a varying cross-sectional area and convert still more kinetic energy to pressure energy.

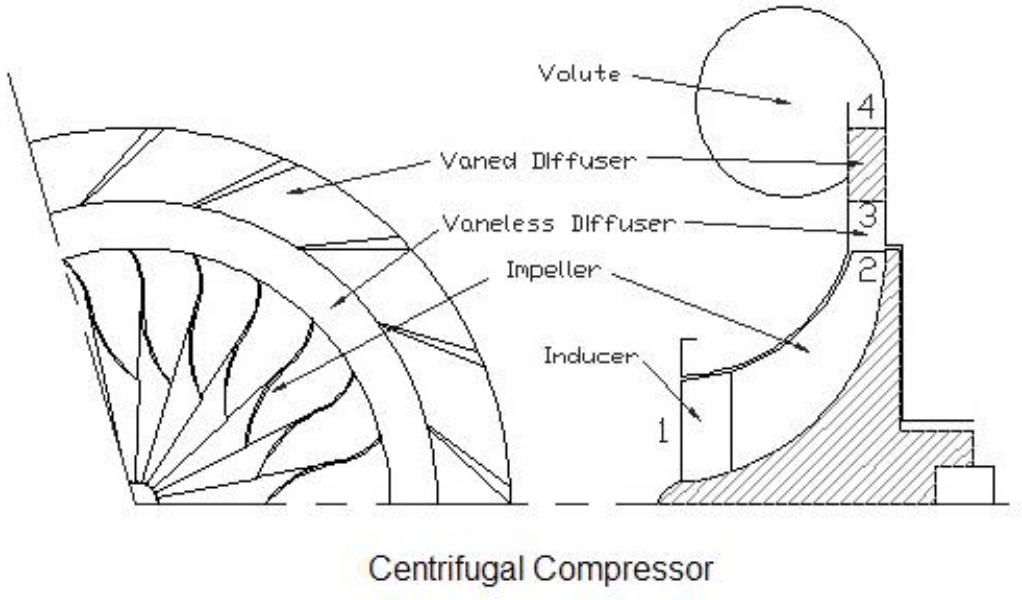

Figure 2.3 Cross-sectional view of centrifugal compressor (Watson and Janota. 1982)

Turbine

Two different types of turbines are used in turbochargers. The axial turbine and radial turbine cross-sectional views are shown in Figure 2.4. From Figure 2.4 the main components of the axial turbine can be identified as the nozzle/stator and rotor. Another component absent in the drawing is the discharge casing. The axial turbine for a turbocharger is similar in characteristics to a single stage of an axial turbine of a gas turbine engine. The axial turbine utilizes an increasing area that is used for the expansion of hot exhaust gases. The expanding exhaust gases pass through the nozzle and rotor causing the rotor to rotate and create shaft work (Watson and Janota. 1982). The discharge casing collects the exhaust gases after passing through the rotor to be expelled. Typically axial turbine turbochargers are used for larger applications such as stationary engines, locomotive engines, and marine engines. Figure 2.4 also identifies the main components of a radial turbine as the inlet casing, nozzle, vaneless space, and rotor. According to Watson and Janota (1982), the inlet casing provides a uniform flow of the exhaust gases to the nozzle. The nozzle is then used to accelerate the flow, thus causing a pressure decrease and an increase in the kinetic energy. The vaneless space is used to allow flow wakes to mix. The rotor is the only component where energy transfer occurs.

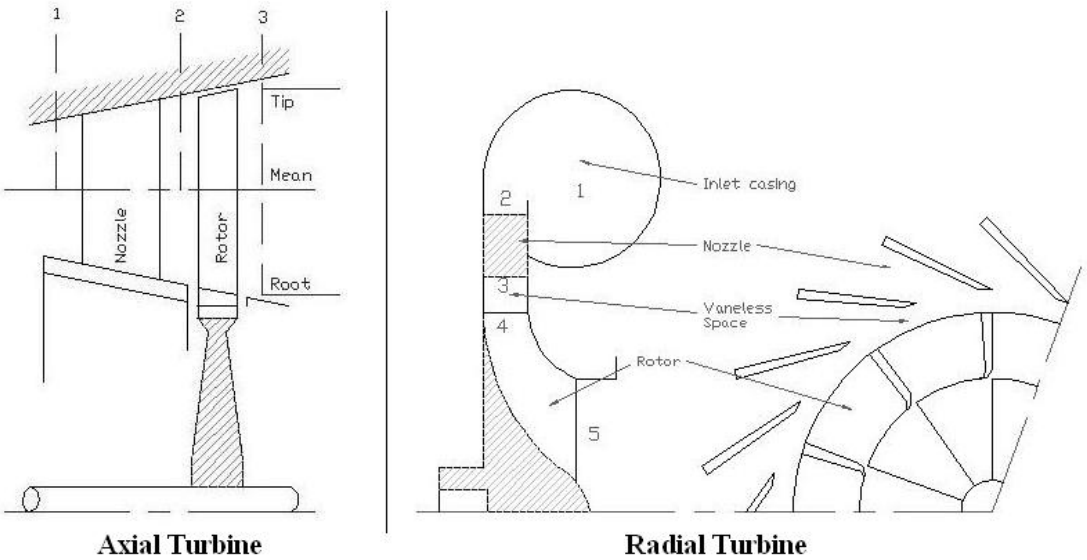

Figure 2.4 Cross-sectional views of axial and radial turbines (Watson and Janota. 1982)

Sealed Compartment

The sealed compartment is the barrier between the turbine and compressor components. The sealed compartment typically contains the connecting shaft between the compressor and turbine, bearings to support the shaft, an oil lubricating system, cooling system, and seals (Baines. 2005). The shaft is supported by bearings that need to run for extended time periods under potentially harsh abuse. The bearings must be able to handle vibrations from unbalanced wheels. The oil system is used to lubricate the bearings. The turbine is subjected to high temperature exhaust gases and to minimize the heat loss to the rest of the turbocharger and extend the life of the turbocharger the casing needs to be cooled with a coolant system. The turbine housing is typically cooled either with water or air. The water-cooled turbines are available for applications when thermal radiation needs to be minimized due to confined spaces of engine compartments of marine ships, locomotives, etc. Some air-cooled turbines can simply be insulated while using a stream of air bled from the compressor to keep the bearing area and turbine housing cool (Watson and Janota. 1982). Seals are at either end of the shaft to keep lubricants from entering the gas path of the compressor and turbine components.

Analysis Techniques

One, two, or three-dimensional models can be used to analyze complex turbocharger flows. For two and three-dimensional models the development and implementation corresponds to a very time consuming process and often these models rely on a performance analysis that encompasses functions of one-dimensional modeling (Aungier. 2000). A one-dimensional approach includes a combination of fundamental fluid flow equations, thermodynamic equations, and empirical relationships (Aungier. 2000). The fluid flow and thermodynamic equations are obtained from Euler's turbomachinery theory and corresponding velocity diagrams. Empirical relationships characterize the losses in the turbocharger and the correlations are obtained from experimental testing thus making one-dimensional models only as accurate as the experimental data from which they are derived. However, the simplicity of the methodology and faster computational speed makes one-dimensional modeling an attractive proposition; thus this approach was used for the modeling in this thesis.

Matching components by experiment is another technique, and is probably the most robust. The downfall is that experimental methods are especially time consuming and very expensive.

Energy Destruction Losses

Energy destruction losses describe the pressure decreases that are seen in a non-isentropic analysis. The literature documents many losses seen by different components throughout the turbocharger system. Each component is subjected to different boundary conditions such as the constant rothalpy (defined as the difference between enthalpy and angular momentum) in the impeller and constant enthalpy in the stationary components, and each component is affected by different losses that account for the boundary conditions applied. Compressor losses are quantified in Figure 2.5 and occur in both the rotating and stationary components of the turbocharger. These losses are due to a variety of physical events, such as clearances, skin friction, incidence, recirculation, and other entropy-generating processes. Losses in rotating parts are more pronounced and impact compressor performance much more than those in stationary components (Aungier. 2000 and Boyce. 2003).

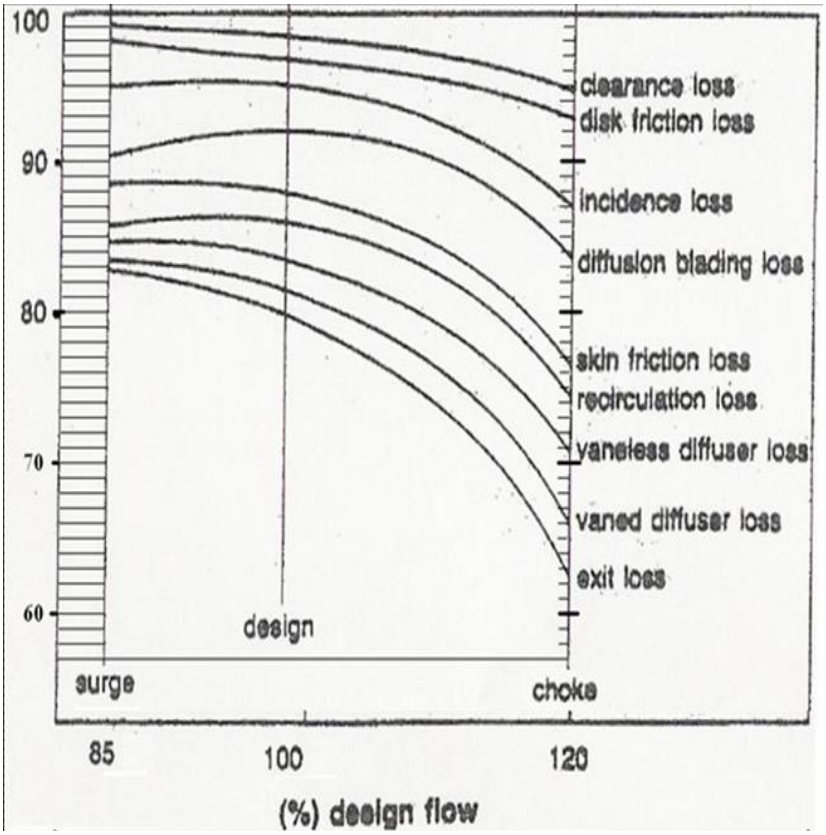

Figure 2.5 Centrifugal compressor losses (Boyce. 2003)

In a number of open literature sources such as Watson and Janota (1982) and Japikse (1996), losses are typically lumped together as a slip factor and/or loss coefficient. The downside of such a treatment is that effects of individual losses are not clearly characterized and thus their influence is poorly understood.

On the other hand, Aungier (2000) and Boyce (2003) documented individual losses in far greater detail then Watson and Janota (1982) and Japikse (1996). Losses itemized by Aungier (2000) were incorporated into this compressor model. The compressor has four components and the losses with the greatest impact on compressor performance are described briefly in Table 2.1 (Aungier. 2000).

Table 2.1 Compressor impeller losses quantified in Figure 2.5

Clearance	Accounts for the flow that escapes the compressor flow path through the clearance gap between the impeller blades and the exterior shroud and has an approximately 1.5 percent effect on compressor performance at design conditions.
Disk friction	Limits the torque coefficient and depends on different flow regimes and roughness of the impeller finish. The torque coefficient for the friction work is split between the disk and the impeller housing and has an approximately 1.5 percent effect on the compressor performance at design conditions.
Incidence loss	Accounts for the flow adjustment of the actual fluid flow to the blade angle at the inlet of the impeller and has an approximately 2.0 percent effect on the compressor performance at design conditions.
Entrance diffusion loss	Accounts for excessive flow diffusion from blade inlet to the throat. The flow diffusion can be greatly affected by the blade thickness at the inlet and has an approximately 3.0 percent effect on the compressor performance at design conditions.
Skin friction loss	The loss from the fluid flowing over the wall, also known as wall friction and has an approximately 4.0 percent effect on the compressor performance at design conditions.
Recirculation	Accounts for the backflow into the impeller exit. The backflow is caused by an increased exit flow angle that then results in flow recirculation causing energy to be returned to the impeller and has an approximately 2.0 percent effect on the compressor performance at design conditions.

Table 2.2 briefly explains other impeller losses described by Aungier (2000) and Boyce (2003) that affect the compressor mean thermodynamic efficiency but were not included in Figure 2.5.

Table 2.2 Compressor impeller losses not quantified in Figure 2.5

Choking loss	Accounts for the Mach number at the throat approaching 1.0.
Blade loading loss	Accounts for the blade-to-blade pressure gradient that produces secondary flows that potentially lead to stall.
Hub to shroud loading loss	Similar to blade loading but accounts for the pressure gradient in the hub-to-shroud direction. This pressure gradient produces secondary flows that can lead to stall.
Blockage loss	Accounts for the mixing of distorted meridional velocities.
Wake mixing loss	Accounts for the mixing of blade wake flows with the free stream flow.
Supercritical Mach number loss	Accounts for the shock wave losses produced by boundary layer separation when blade surface velocities reach supersonic conditions.

The vaneless diffuser energy destruction losses are skin friction and diffusion (Aungier, 2000). Aungier (2000) explains that the skin friction losses have the greatest affect and that as the vaneless diffuser radius increases the skin friction also increases. The flow in the vaneless diffuser follows a spiraling path to the vaned diffuser.

The vaned diffuser also exhibits energy destruction losses associated with skin friction, incidence angle, blockage, wake mixing, and choking that are very similar to the impeller conditions. The explanation of the vaned diffuser losses is identical to that described in Tables 2.1 and 2.2.

The volute suffers from skin friction losses and the additional energy destruction losses described in Table 2.3.

Table 2.3 Compressor volute losses (Aungier. 2000)

Meridional velocity head loss	Recovering the meridional velocity is impossible and this velocity becomes a swirling condition within the volute passage that is eventually dissipated downstream.
Tangential velocity head loss	Part of the tangential velocity head is expected to be lost when the area and mean radius variation in the circumferential direction forces a change in angular momentum.
Exit cone loss	The performance of the cone matches that of an optimized ideal conical diffuser.

The losses described above are the losses used in modeling to perform a compressor analysis. According to Aungier (2000), Boyce (2003), Watson and Janota (1982), and others, skin friction losses are typically the greatest and are a function of the Reynolds number, surface finish, and flow rate. When the turbocharger operates at off-design conditions, the next greatest effect on the mean thermodynamic efficiency is the incidence loss due to the flow path of the air passing through the compressor not matching the blade angles. The incidence losses are seen in the impeller and in the vaned diffuser. Calculation of the losses and understanding the cause can be used to redesign the compressor components to increase the overall mean thermodynamic efficiency of the compressor.

Compressor Performance

Compressor performance is typically presented as a "map" of the compressor mass flow rate, pressure ratio, and mean isentropic thermodynamic efficiency. Figure 2.6 is an example of a compressor performance map. The horizontal axis represents the air mass flow rate and the vertical axis represents the pressure ratio across the compressor. Lines of constant compressor speed are shown as indicated in Figure 2.6.

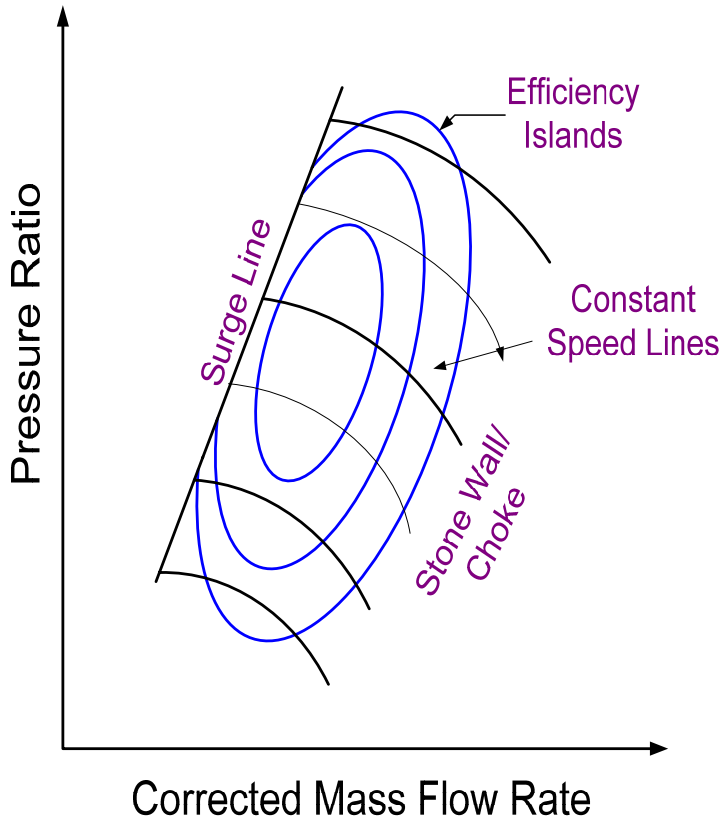

Figure 2.6 Compressor map (Watson and Janota. 1982)

There are three zones of a compressor map. The central area is the stable operating zone and where the highest turbocharger efficiency occurs. The area to the left of the stable zone is an unstable zone separated from the stable zone by the surge line. Surge according to Watson and Janota (1982) can be described as when the mass flow rate decreases while the pressure ratio is held constant until a point in the scenario is reached when a flow reversal occurs in the boundary layers resulting in lower efficiency and instability. If the mass flow rate decreases further, a complete flow reversal causes a relief in the pressure gradient until a lower pressure ratio and stable condition is achieved. The flow then builds up to the initial conditions again causing the flow reversal. This process continues at a fixed frequency. The turbocharger should not be operated in the surge zone due to instability. The area to the right of the stable zone is the choking zone. The choke zone occurs when a maximum mass flow rate for the compressor flow area has been reached (Watson and Janota. 1982). The mass flow rate can only be increased

with higher compressor speeds. Compressor maps are a convenient way to display compressor performance.

Variable Geometry Turbocharger

The Variable Geometry Turbocharger (VGT) was designed and tested by the researchers at the National Gas Machinery Laboratory (NGML). According to Chapman et al. (2007), the operating ranges of a turbocharger compressor is limited by the surge and choke flow conditions that define its operating range at low and high flow-rates, respectively. In general, conventional vaned diffusers lead to an improvement in efficiency and pressure ratio compared to a diffuser without vanes, but the operating range is reduced. This occurs because a conventional full length vaned diffuser creates a throat that acts as a blockage and thereby reduces the flow range. In addition, incidence effects at low flow rates can have an adverse effect on the surge condition. The deficiency in the operating range can be eliminated by the adoption of variable geometry diffusers (Chapman et al. 2007).

The VGT is designed based on a turbocharger model ET18md2v (Chapman et al. 2007). The ET 18 model was modified to create the VGT. The VGT's vaned diffuser blades can be rotated in real time to increase the operating range of the turbocharger under loading conditions. By adjusting the VGT diffuser vane position the compressor performance map is moved so that the engine load curve remains at optimum conditions. The diffuser vanes are adjusted so the blade angle aligns with the flow angle, thus creating lower incidence losses and improved turbocharger operation (Chapman et al. 2007). For a more detailed description of the concepts behind the development and design of the VGT, refer to the report "Variable Geometery Turbocharger" published in 2007 and submitted to the Pipeline Research Council International, Inc. by the National Gas Machinery Laboratory.

Drawings of the VGT design are shown in Figures 2.7 and 2.8. Figure 2.7 shows and labels the VGT turbo in an extruded view.

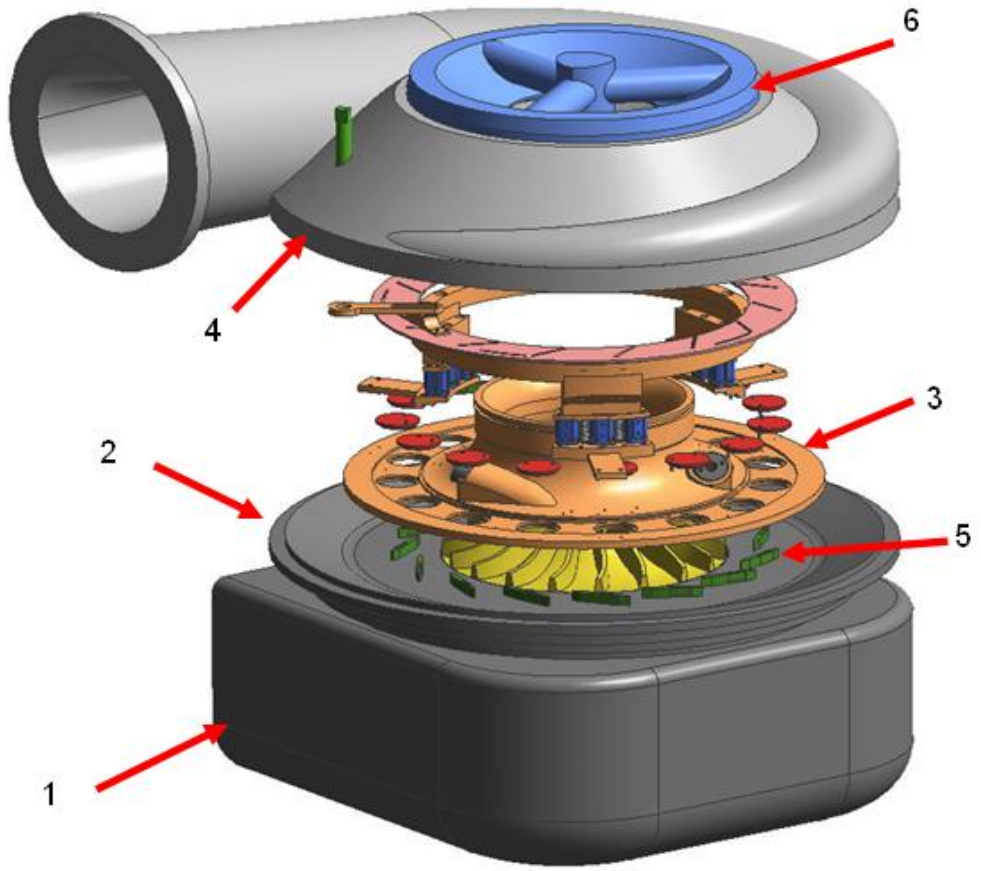

1	Blower inlet
2	Back plate
3	Diffuser
4	Blower discharge casing
5	Vanes (15 pieces)
6	Blower Inlet Casing

Figure 2.7 Complete extrusion of the VGT compressor (Chapman et al. 2007)

Figure 2.8 shows and labels the extruded view of the VGT internal parts. The groove ring (part 8) is rotated through a rotational shaft with an arm and connection pad (parts 10 – 12). The ring has several grooves, in which a pin on the washer (part 9) slides along. While rotating the groove ring, the washers get rotated. There is a second pin on the bottom side of the washer. The second pin goes into the groove in the vane and rotates the vane.

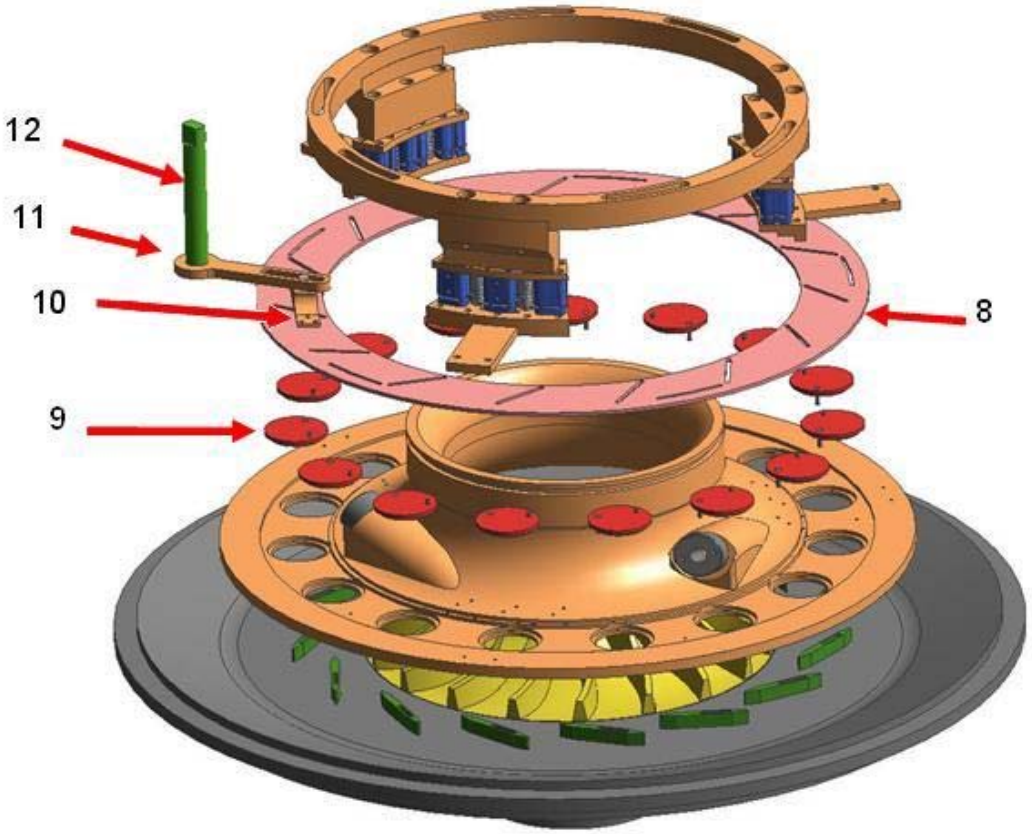

8	Groove ring
9	Vane washer
10	Rotation connection
11	Shaft arm
12	Turning shaft

Figure 2.8 Additional VGT parts (Chapman et al. 2007)

Literature Review Summary

The two popular configurations of a turbocharger are a turbocharger with a centrifugal compressor and radial turbine or a turbocharger with a centrifugal compressor and axial turbine. Turbochargers typically use a centrifugal compressor because an axial compressor requires several stages to accomplish the pressure rise a single staged centrifugal compressor can generate. The turbocharger can be separated into three man components, compressor, turbine, and sealed compartment. A turbocharger is a compressor driven by a turbine with the connecting shaft supported by bearings in the

sealed compartment. There are many energy destruction losses in a compressor and the compressor losses can be separated into each individual component. The losses can be analyzed individual to produce improved thermodynamic compressor efficiency. Compressor performance can be measured and mapped as the pressure ratio dependent on the mass flow rate for different rotational speeds. Compressor performance maps are separated into three zones, the stable zone located between the unstable surge zone and the choking zone where flow is limited by the flow area. The VGT is a turbocharger designed and built by the researchers at the NGML and uses a varying vane position vaned diffuser to increase the operating range of a compressor for different loading situations.

CHAPTER 3 - Compressor mathematical description

Typically, parameters are measured at the compressor inlet and compressor discharge. Unfortunately, to design higher performance compressors, parameter measurements should be taken for each individual component of the compressor. Because taking individual component measurements is not likely to happen due to the difficulty and expense, a mathematical modeling solution is required to calculate the parameters. The following pages describe each compressor component mathematically.

Component Description from a Mathematical Standpoint

Each component is described mathematically by the generalized approach shown in Figure 3.1. A set of equations and associated variables fully describes a component. Variables that influence the component are either at the component inlet, such as the inlet pressure, inlet temperature, and inlet velocities or at the component exit, such as the exit pressure, exit temperature, and exit velocities, or across the component, such as the component efficiency and work consumption. The generalized approach also includes a set of algebraic equations that relate the input and output conditions. The development of the generalized component approach simplified the development of the overall mathematical description.

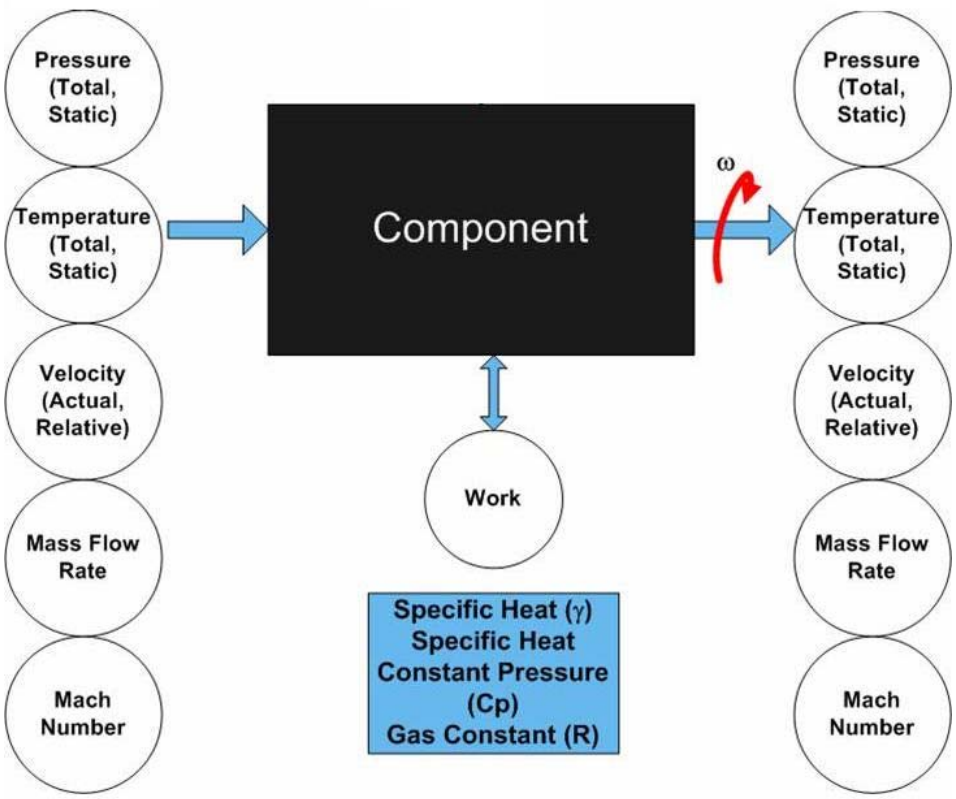

Figure 3.1 Generalized component-based mathematical approach (Sengupta et al. 2007)

Figure 3.2 shows the cross-sectional schematic of the centrifugal compressor. For modeling purposes the compressor is separated into its individual components. The component inlet and exit characteristics are defined as stations. The stations are located at the component inlets and exits because one-dimensional relationships that describe the compressor utilize the inlet and exit conditions. The compressor can be described using five stations. Station one is the impeller inlet and Station two is the impeller exit and vaneless diffuser inlet. The conditions for the impeller exit and vaneless diffuser inlet are the same. Station three is the vaneless diffuser exit and vaned diffuser inlet. Again, the vaneless diffuser exit and vaned diffuser inlet have the same conditions. Station four is the vaned diffuser exit and volute inlet and the conditions are equal. Station five is the volute exit condition but is not labeled in Figure 3.2 because it does not occur in the plane of the diagram.

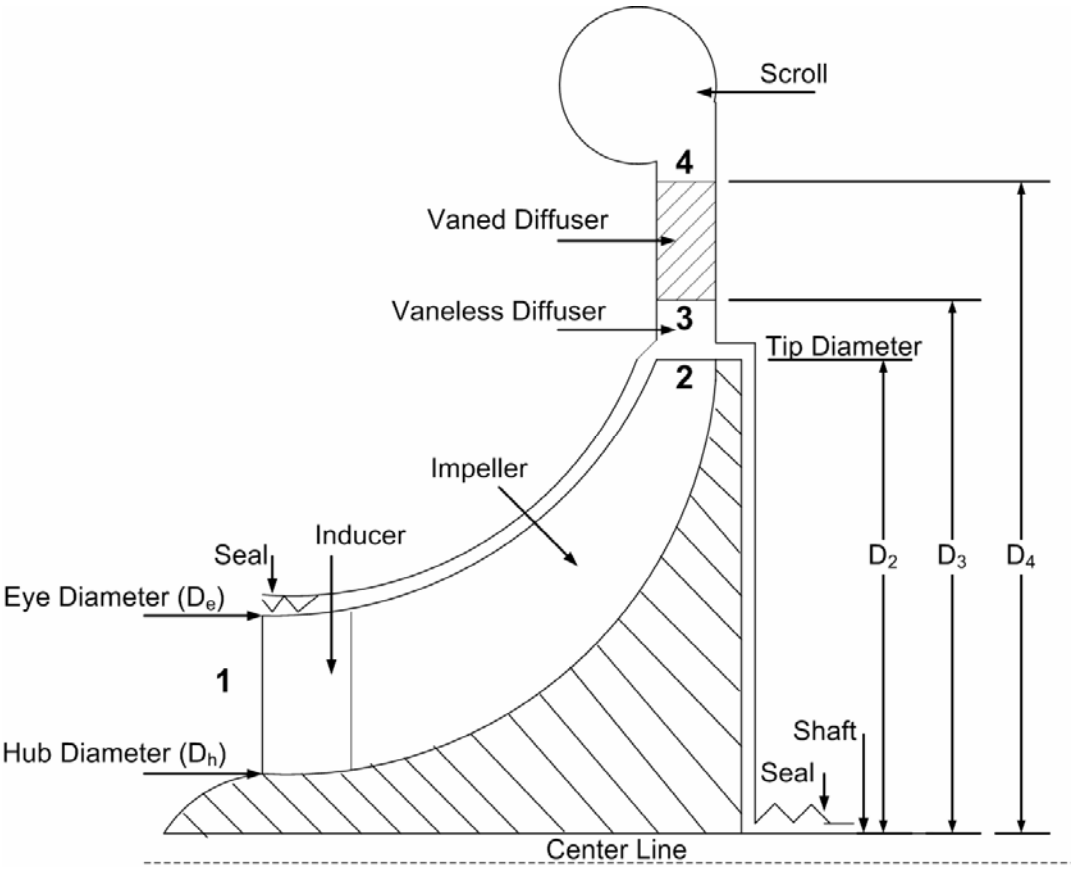

Figure 3.2 Compressor cross-section labeling the stations (Boyce. 2003)

The compressor components were developed, as described in the next section, using a sufficient number of equations to capture the detail of the impact of geometry, clearances, surface conditions, inlet conditions, and operating parameters. The equations were developed from the moment of momentum equation, steady flow energy equation, mass continuity equation, thermodynamic equation of state, and trigonometric relations from corresponding velocity vector diagrams at the mean stream line. When solved as a system of equations, they result in the representative thermodynamic state of air (i.e., pressure, temperature, velocity, and Mach number) throughout the turbocharger compressor.

Component Mathematical Parameters

Mathematically the performance parameters need to be developed for each component. The parameters needed for each component are mean isentropic thermodynamic efficiency, power consumption, fluid density, and pressure losses. To

calculate the component performance parameters, unknown and known inlet and discharge conditions for each component must be determined. The unknown inlet and discharge conditions that need to be calculated are the pressure, temperature, velocity, flow angle, Mach number, and air density. The unknown component inlet and exit conditions can be calculated using the known conditions. The known conditions are the ambient static pressure, ambient static temperature, air mass flow rate, turbocharger rotational speed, and turbocharger geometry. The known conditions can all be measured during operation.

Mean Isentropic Efficiency Parameter

The component parameter mean isentropic thermodynamic efficiency is a function of compressor inlet and exit total (the sum of the static and dynamic condition) pressure and total temperature and is mathematically described as (Nunn. 1989):

$$\eta = \frac{\left(\frac{p_{t,out}}{p_{t,in}}\right)^{\frac{\gamma-1}{\gamma}} - 1}{\left(\frac{T_{t,out}}{T_{t,in}}\right) - 1} \tag{3.1}$$

The inlet and exit total pressure and total temperature need to be calculated for each compressor component. The inlet and exit total temperature can be computed from compressible relationships and are mathematically described as (Nunn. 1989):

$$T_t = T_s\left[1 + \left(\frac{\gamma-1}{2}\right)M^2\right] \tag{3.2}$$

The total temperature is a function of the Mach number which is a function of the speed of sound and absolute velocity. The Mach number and speed of sound are mathematically described as (Mattingly. 1996):

$$M = \frac{C}{a} \tag{3.3}$$

$$a = \sqrt{\gamma R_g T_s} \tag{3.4}$$

The inlet and exit total pressure is also a computed using compressible relationships and are mathematically described as (Nunn. 1989):

$$p_t = p_s\left[1+\left(\frac{\gamma-1}{2}\right)M^2\right]^{\frac{\gamma}{\gamma-1}} \tag{3.5}$$

Power Consumption Parameter

Compressor power consumption can be described using Euler's turbomachinery equation. Euler's equation is the combination of basic energy conservation and conservation of angular momentum which provides compressor power in terms of the tangential velocity. The relationship is mathematically described as:

$$h_{t,out} - h_{t,in} = \omega\left(r_{out}C_{U,out} - r_{in}C_{U,in}\right) \tag{3.6}$$

Because power consumption for each component is needed, now the inlet and exit tangential velocities need to be calculated. To calculate the tangential velocities for the impeller the velocity diagrams in Figures 3.3 and 3.4 are used.

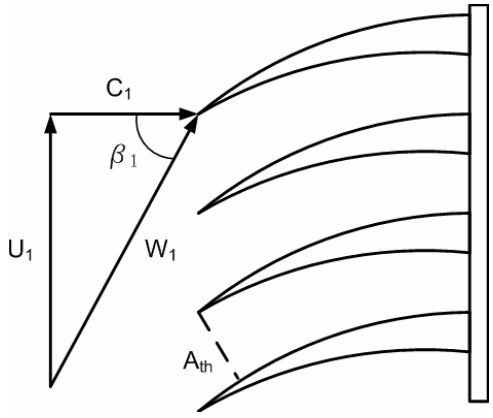

Figure 3.3 Impeller inlet velocity diagram (Boyce. 2003)

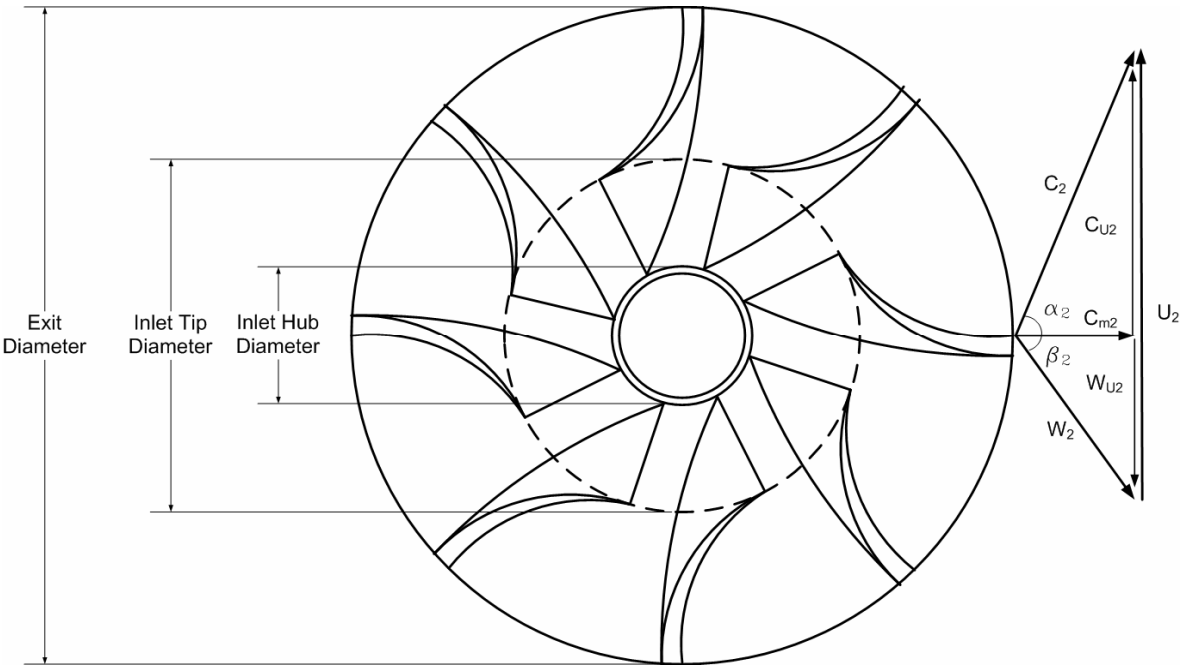

Figure 3.4 Impeller exit velocity diagram (Boyce. 2003)

Figure 3.3 shows the velocity diagram for the impeller inlet. At the impeller inlet an assumption is made that the absolute flow is only axial. Therefore, the absolute flow angle is zero with respect to the axis. Figure 3.3 shows that at the inlet of the impeller there is no absolute tangential velocity vector. However, because the impeller is rotating the velocity diagram shows that the impeller inlet is subjected to relative velocity vectors. The relative velocities are a function of the relative flow angle and can be mathematically described as (Bathie. 1996):

$$C_1 = W_1 \cos(\beta_1) \tag{3.7}$$

$$W_{U1} = W_1 \sin(\beta_1) \tag{3.8}$$

The blade velocity at the impeller inlet is equal to the relative tangential velocity vector. The blade velocity is a function of the rotational speed (N) of the compressor and is mathematically described as (Mattingly. 1996):

$$U_1 = \frac{2\pi N}{60} r_1 \tag{3.9}$$

Figure 3.4 shows the velocity vector diagram that describes the impeller exit characteristics. At the exit of the impeller the flow is radial and no longer axial. The velocity vectors of the absolute and relative velocities are functions of the absolute and relative flow angles respectively, and are mathematically describe as (Bathie. 1996):

$$C_{m2} = C_2 \cos(\alpha_2) \tag{3.10}$$

$$C_{U2} = C_2 \sin(\alpha_2) \tag{3.11}$$

$$C_{m2} = W_2 \cos(\beta_2) \tag{3.12}$$

$$W_{U2} = W_2 \sin(\beta_2) \tag{3.13}$$

$$U_2 = C_{U2} + W_{U2} \tag{3.14}$$

The diffuser and volute components are not in the rotating frame of reference so velocity diagrams would only show the absolute velocity vectors.

The mass flow rate for the components is a function of the meridional velocity, fluid density, and cross-sectional area. The relationships between these parameters are mathematically described as (Cohen, et al.. 1987):

$$\dot{m} = C_m \rho_s A \tag{3.15}$$

$$\rho_s = \frac{p_s}{R_g T_s} \tag{3.16}$$

Loss Parameters

The non-dimensional loss parameters $(\bar{\omega})$ of the components are computed as functions of the geometry, velocity, temperature, and pressure. The loss parameters for each component are different. The following sections individually describe each component loss parameter.

Impeller

The non-dimensional losses of the impeller are developed in the rotating frame of reference and are converted into a total relative pressure loss described as (Aungier. 2000):

$$\Delta p_{tr} = f_c \left(p_{tr1} - p_{s1} \right) \sum_i \bar{\omega}_i \tag{3.17}$$

The total relative pressure loss is corrected using a correction factor $\left(f_c \right)$ which is a function of the total relative density $\left(\rho_{tr} \right)$. The correction factor and the total relative density are mathematically described as (Aungier. 2000):

$$f_c = \frac{\rho_{tr2} T_{tr2}}{\rho_{tr1} T_{tr1}} \tag{3.18}$$

$$\rho_{tr} = \frac{p_{tr}}{R_g T_{tr}} \tag{3.19}$$

The impeller component is the only component of the compressor that is based in the relative frame of reference. Because the impeller is in the relative frame of reference, the total relative pressure and total relative temperature need to be determined from the compressible relationships and are mathematically described as (Nunn. 1989):

$$p_{tr} = p_s \left[1 + \left(\frac{\gamma - 1}{2} \right) M_r^2 \right]^{\frac{\gamma}{\gamma - 1}} \tag{3.20}$$

$$T_{tr} = T_s \left[1 + \left(\frac{\gamma - 1}{2} \right) M_r^2 \right] \tag{3.21}$$

The total relative pressure and total relative temperature are functions of the relative Mach number which is mathematically described as (Mattingly. 1996):

$$M_r = \frac{W}{a} \tag{3.22}$$

To calculate the non-dimensional loss parameters in the impeller, isentropic conditions are determined first. The losses are then applied to the isentropic conditions to

calculate the actual conditions. The non-isentropic parameters are evaluated with the assumption that rothalpy is conserved. Rothalpy is defined as the difference between the total enthalpy and angular momentum, and is mathematically described as (Aungier. 2000):

$$R = h_t - NrC_U \tag{3.23}$$

Conservation of rothalpy requires that the isentropic relative total temperature is equal the actual relative total temperature. The actual total relative pressure at the impeller exit is the difference between the isentropic total relative pressure and the total relative pressure loss, mathematically described as (Aungier. 2000):

$$p_{tr2} = p_{tr2,id} - \Delta p_{tr} \tag{3.24}$$

The impeller loss parameters are functions of the inlet conditions, throat conditions, isentropic exit conditions, and boundary conditions. The impeller boundary conditions are the area and radius for the respective station, mass flow rate, and rotational speed. Mass flow rate and rotational speed are constant throughout the entire compressor.

The inlet conditions are calculated using the velocity diagrams, total pressure relationships, total temperature relationships, total relative pressure relationships, total relative temperature relationships, density, and the assumption that the absolute flow is in the axial direction. The impeller throat is the point in the impeller when the smallest area occurs. Typically the throat is near the impeller inlet. The throat conditions are calculated using the velocity diagrams, total pressure relationships, total temperature relationships, total relative pressure relationships, total relative temperature relationships, density, and inlet-exit interaction conditions. The inlet-exit interactions are isentropic and use the Euler turbomachinery equations. The inlet-exit interactions applied across the

throat area are described by the following equations (Bathie. 1996):

$$T_{tTh} = T_{t1} - \left[\frac{2N\pi \left(C_{U1} r_{m1} - C_{UTh} r_{mTh} \right)}{60 c_p} \right] \tag{3.25}$$

$$p_{tTh} = p_{t1} \left(\frac{T_{tTh}}{T_{t1}} \right)^{\frac{\gamma}{\gamma - 1}} \tag{3.26}$$

Isentropic impeller exit conditions are used in the calculation of the impeller loss parameters. The impeller exit conditions are calculated using velocity diagrams, total pressure relationships, total temperature relationships, total relative pressure relationships, total relative temperature relationships, fluid density, and the assumption that the impeller exit relative flow angle (β_2) follows the impeller exit blade angle due to no slip in the isentropic situation. Slip is a condition in the loss parameters and is discussed later.

Once the isentropic exit conditions are calculated, the next step is to compute the loss parameters throughout the compressor impeller. The non-dimensional losses for the impeller are calculated in a relative frame of reference and converted into a pressure reduction. According to Auniger (2000) and Boyce (2003) there are 11 well-documented losses that affect the impeller, these losses were described in Tables 2.1, 2.2, and 2.3 of Chapter 2. The losses that affect the impeller are:

1. Shock
2. Incidence
3. Diffusion
4. Choke
5. Skin friction
6. Clearance gap
7. Blade loading
8. Hub-shroud loading
9. Wake mixing
10. Expansion
11. Supercritical Mach number

The equations for each loss require separate calculations and boundary conditions. The non-dimensional loss equations and boundary conditions are descried extensively in the following pages and come primarily from Aungier (1993 and 2000) and Boyce (2003). The shock loss equation is described mathematically as (Aungier. 1993 and 2000):

$$\bar{\omega}_{Sh} = 1 - \left(\frac{W_{1Th}}{W_1}\right)^2 - \left(\frac{2}{(\gamma - 1) M_{r1}^2}\right)\left[\left(\frac{p_{1Th}}{p_{s1}}\right)^{\frac{\gamma-1}{\gamma}} - 1\right] \tag{3.27}$$

The incidence loss equation is described mathematically as (Aungier. 1993 and 2000):

$$\bar{\omega}_{Inc} = 0.8\left[1 - \frac{C_{m1}}{W_1 \sin(\theta_{m1})}\right]^2 + \left[\frac{t_{b1} Z}{2\pi r_{m1} \sin(\theta_{m1})}\right]^2 \tag{3.28}$$

The diffusion loss has a constraint that requires it to be greater than or equal to zero and is described mathematically as (Aungier. 1993 and 2000):

$$\bar{\omega}_{Diff} = 0.8\left[1 - \frac{W_{1Th}}{W_1}\right]^2 - \bar{\omega}_{Inc};\ \left(\bar{\omega}_{Diff} \geq 0\right) \tag{3.29}$$

The choke loss requires the calculation of a contraction ratio (C_r) and a constraint condition (X). The constraint condition must be greater than zero; otherwise the choke loss is zero. The choke loss, contraction ratio, and constraint condition are described mathematically as (Aungier. 1993 and 2000):

$$\bar{\omega}_{CH} = \frac{1}{2}\left(0.05X + X^7\right) \tag{3.30}$$

$$X = 11 - \frac{10 C_r A_{Th}}{A^*};\ \left(X > 0\right) \tag{3.31}$$

$$C_r = \sqrt{\frac{A_1 \sin(\theta_{m1})}{A_{Th}}} \tag{3.32}$$

The skin friction loss incorporates the losses created be the resistance of air over the surface area, thus skin friction depends on a Reynolds number, hydraulic diameter $\left(D_H\right)$, and friction coefficient $\left(c_f\right)$ (Boyce. 2003):

$$D_H = \frac{\frac{\pi}{2}\cos\left(\theta_{m1}\right)\left(D_{1tip}^2 - D_{1hub}^2\right)}{\pi\cos\left(\theta_{m1}\right)\left(D_{1tip} + D_{1hub}\right) + 2Z\left(D_{1tip} - D_{1hub}\right)} + \frac{\pi D_2 b_2 \cos\left(\theta_2\right)}{\pi D_2 \cos\left(\theta_2\right) + Zb_2} \tag{3.33}$$

$$\mathrm{Re}_d = \frac{\rho C D_H}{\mu} \tag{3.34}$$

The friction coefficient will apply to every component of the compressor, thus a general set of equations is developed that depends on the Reynolds number, hydraulic diameter, and surface roughness $\left(e\right)$. The friction coefficient developed by Aungier (2000) has constraint conditions that determine if laminar or turbulent conditions apply. For laminar conditions the friction coefficient is described mathematically as:

$$c_f = c_{fl} = \frac{16}{\mathrm{Re}_d};\ \left(\mathrm{Re}_d < 2{,}000\right) \tag{3.35}$$

For turbulent flow over smooth surfaces the fiction coefficient relies on:

$$\frac{1}{\sqrt{4c_{fts}}} = -2\log_{10}\left[\frac{2.51}{\mathrm{Re}_d\sqrt{4c_{fts}}}\right];\ \left(\mathrm{Re}_d > 2{,}000\right) \tag{3.36}$$

For turbulent flow over rough surfaces the friction coefficient relies on:

$$\frac{1}{\sqrt{4c_{ftr}}} = -2\log_{10}\left[\frac{e}{3.71D_H}\right];\ \left(\mathrm{Re}_d \geq 2{,}000\right) \tag{3.37}$$

Surface roughness (measured input variable) becomes relevant when:

$$\mathrm{Re}_e = \frac{\left(\mathrm{Re}_d - 2{,}000\right)e}{D_H} > 60 \tag{3.38}$$

Thus, the friction coefficient for turbulent conditions is described mathematically as:

$$c_f = c_{ft} = c_{fts}; \quad \begin{matrix}(\mathrm{Re}_e < 60) \\ (\mathrm{Re}_d > 4{,}000)\end{matrix} \tag{3.39}$$

$$c_f = c_{ft} = c_{fts} + \left(c_{ftr} - c_{fts}\right)\left(1 - \frac{60}{\mathrm{Re}_e}\right); \quad \begin{matrix}(\mathrm{Re}_e \geq 60) \\ (\mathrm{Re}_d > 4{,}000)\end{matrix} \tag{3.40}$$

$$c_f = c_{fl} + \left(c_{ft} - c_{fl}\right)\left(\frac{\mathrm{Re}_d}{2{,}000} - 1\right); \quad (2{,}000 < \mathrm{Re}_d < 4{,}000) \tag{3.41}$$

The skin friction loss equation is described mathematically as (Aungier. 1993 and 2000):

$$\bar{\omega}_{SF} = 4c_f \left(\frac{\bar{W}}{W_1}\right)^2 \frac{L_B}{D_H} \tag{3.42}$$

$$\bar{W}^2 = \frac{\left(W_1^2 + W_2^2\right)}{2} \tag{3.43}$$

The clearance gap loss is a function of the clearance gap leakage flow rate $\left(\dot{m}_{CL}\right)$. The clearance gap leakage flow rate is a function of the velocity of the leakage flow $\left(U_{CL}\right)$. The velocity of the leakage flow is a function of the pressure difference across the gap $\left(\Delta p_{CL}\right)$. The clearance gap loss and its conditions are described mathematically as (Aungier. 1993 and 2000):

$$\bar{\omega}_{CL} = \frac{2\dot{m}_{CL}\Delta p_{CL}}{\dot{m}\rho_1 W_1^2} \tag{3.44}$$

$$\dot{m}_{CL} = \rho_2 ZsLU_{CL} \tag{3.45}$$

$$U_{CL} = 0.816\sqrt{\frac{2\Delta p_{CL}}{\rho_2}} \tag{3.46}$$

$$\Delta p_{CL} = \frac{\dot{m}\left(r_2 C_{U2} - r_{m1} C_{U1}\right)}{Z\bar{r}\bar{b}L} \tag{3.47}$$

$$\bar{r} = \frac{r_{m1} + r_2}{2} \tag{3.48}$$

$$\bar{b} = \frac{b_1 + b_2}{2} \tag{3.49}$$

The blade loading loss requires the calculation of the blade work coefficient $\left(I_B\right)$ which is described later in the chapter. Blade loading loss is described mathematically as (Aungier. 1993 and 2000):

$$\bar{\omega}_{BL} = \frac{\left(\Delta W / W_1\right)^2}{24} \tag{3.50}$$

$$\Delta W = \frac{2\pi D_2 U_2 I_B}{Z L_B} \tag{3.51}$$

The blade work coefficient $\left(I_B\right)$ is a function of the impeller exit flow coefficient $\left(\phi_2\right)$, the slip factor $\left(\sigma\right)$, and tip distortion factor $\left(\lambda\right)$. The blade work coefficient and exit flow coefficient are described mathematically as (Aungier. 1993 and 2000):

$$I_B = \sigma\left(1 - \lambda\phi_2 \cot\left(\theta_2\right)\right) - \frac{U_1 C_{U1}}{U_2^2} \tag{3.52}$$

$$\phi_2 = \frac{\dot{m}}{\rho_2 A_2 U_2} \tag{3.53}$$

The slip factor has constraint conditions and multiple calculations. If the impeller radius ratio $\left(\varepsilon\right)$ is greater than the impeller radius ratio limit $\left(\varepsilon_{LIM}\right)$, then the slip factor needs to be corrected. Otherwise the slip factor in Equation 3.54 is correct. The slip factor and constraints are mathematically described as (Aungier. 1993 and 2000):

$$\sigma = 1 - \frac{\sqrt{\sin\left(\theta_2\right)}\sin\left(\alpha_{C2}\right)}{Z^{0.7}} \tag{3.54}$$

$$\varepsilon = \frac{r_1}{r_2} \tag{3.55}$$

$$\varepsilon_{LIM} = \frac{\sigma - \sigma^*}{1 - \sigma^*} \tag{3.56}$$

$$\sigma^* = \sin\left(19° + 0.2\theta_2\right) \tag{3.57}$$

$$\sigma_{corr} = \sigma\left[1 - \left(\frac{\varepsilon - \varepsilon_{LIM}}{1 - \varepsilon_{LIM}}\right)^{\sqrt{\frac{\theta_2}{10}}}\right] \tag{3.58}$$

The tip distortion factor (λ) is a function of the tip blockage equation (B_2). The tip block equation uses velocity pressure (p_v) and a passage area ratio (A_R). The tip distortion, blockage equation, velocity pressure and passage area ratio are described mathematically as (Aungier. 1993 and 2000):

$$\lambda = \frac{1}{1 - B_2} \tag{3.59}$$

$$B_2 = \bar{\omega}_{SF} \frac{p_{v1}}{p_{v2}} \sqrt{\frac{W_1 D_H}{W_2 b_2}} + \left[0.3 + \frac{b_2^2}{L_B^2} \right] \frac{A_R^2 \rho_2 b_2}{\rho_1 L_B} + \frac{s}{2 b_2} \tag{3.60}$$

$$p_v = p_t - p_s \tag{3.61}$$

$$A_R = \frac{A_2 \sin(\theta_2)}{A_1 \sin(\theta_{1Th})} \tag{3.62}$$

The expansion loss, also known as the blockage loss equation, is described mathematically as (Benedict, et al. 1966):

$$\bar{\omega}_{\lambda} = \left[\frac{(\lambda - 1) C_{m2}}{W_1} \right]^2 \tag{3.63}$$

The hub-to-shroud loss is a function of the passage curvature $(\bar{\kappa}_m)$ and an average of the relative velocities and is described mathematically as (Aungier. 1993 and 2000):

$$\bar{\omega}_{HS} = \frac{\left(\bar{\kappa}_m \bar{b} \bar{W} / W_1 \right)^2}{6} \tag{3.64}$$

The passage curvature is a function of the hub cone angle at the inlet (α_{C1}) and exit (α_{C2}) of the impeller. Passage curvature and the average relative velocity are described mathematically as (Aungier. 1993 and 2000):

$$\bar{\kappa}_m = \frac{\alpha_{C2} - \alpha_{C1}}{L} \tag{3.65}$$

$$\bar{W} = \frac{W_1 + W_2}{2} \tag{3.66}$$

The wake-mixing loss requires that a constraint condition be applied to the relative separation velocity $\left(W_{SEP}\right)$ that is calculated using the equivalent diffusion ratio $\left(D_{eq}\right)$. The equivalent diffusion factor equation is (Lieblein. 1959):

$$D_{eq} = \frac{W_{\max}}{W_2} \tag{3.67}$$

$$W_{\max} = \frac{W_1 + W_2 + \Delta W}{2} \tag{3.68}$$

The constraint condition applied to the relative separation velocity requirement is described mathematically as (Aungier. 1993 and 2000):

$$W_{SEP} = W_2;\ \left(D_{eq} \le 2\right) \tag{3.69}$$

$$W_{SEP} = \frac{W_2 D_{eq}}{2};\ \left(D_{eq} > 2\right) \tag{3.70}$$

The wake-mixing loss is described mathematically as (Aungier. 1993 and 2000):

$$\bar{\omega}_{MIX} = \left[\frac{C_{m,wake} - C_{m,mix}}{W_1}\right]^2 \tag{3.71}$$

$$C_{m,wake} = \sqrt{W_{SEP}^2 - W_{U2}^2} \tag{3.72}$$

$$C_{m,mix} = \frac{C_{m2} A_2}{\pi D_2 b_2} \tag{3.73}$$

The supercritical Mach number loss is a function of the critical Mach number $\left(M_{CR}\right)$ and both are described mathematically as (Aungier. 1993 and 2000):

$$\bar{\omega}_{SCMN} = 0.4\left[\frac{\left(M_{r1} - M_{CR}\right) W_{\max}}{W_1}\right]^2 \tag{3.74}$$

$$M_{CR} = \frac{M_1 W^*}{W_{\max}} \tag{3.75}$$

The isentropic solution is used in conjunction with the loss models to evaluate the non-isentropic or actual conditions. The actual exit conditions can be used to determine the component mean thermodynamic efficiency and power consumption parameters.

The impeller is the only component of the compressor that uses a rotating frame of reference. The following components of the centrifugal compressor are in the stationary form and their calculations coincide. For stationary components rothalpy is reduced to constant enthalpy because conservation of angular momentum is equal to zero due to no rotational speed. Constant enthalpy implies that the total temperature throughout the rest of the components is now constant.

Vaneless Diffuser

The non-dimensional loss parameter for the vaneless diffuser is converted into a total pressure loss. The total pressure loss conversion can be mathematically described as (Aungier. 2000):

$$\Delta p_{t3} = (p_{t2} - p_{s2}) \sum_i \bar{\omega}_i \tag{3.76}$$

The vaneless diffuser loss parameters use a similar approach as in the impeller. The vaneless diffuser requires the calculation of the isentropic conditions to evaluate the loss parameters. The vaneless diffuser inlet conditions have been calculated as being equal to the impeller actual exit conditions. The vaneless diffuser isentropic conditions are calculated using the absolute velocity diagram, total temperature relationships, total pressure relationships, fluid density, and a correlation developed by Japikse (1996) that relates the inlet and exit absolute velocities. The correlation is mathematically described as (Japikse, 1996):

$$\frac{C_2}{C_1} = \left(\frac{D_1}{D_2} \right)^{1.25} \tag{3.77}$$

Aungier (1988 and 2000) described two loss parameters for the vaneless diffuser. The loss parameters are skin fiction and diffusion. The skin friction is a function of the friction coefficient that was developed in the previous impeller section and described

with equations 3.34 through 3.41. The vaneless diffuser skin friction loss parameter is mathematically described as (Aungier. 1988 and 2000):

$$\bar{\omega}_{SF} = 4c_f \left(\frac{\bar{C}}{C_2} \right)^2 \frac{(r_3 - r_2)}{D_{hyd}} \tag{3.78}$$

Aungier's (1988 and 2000) diffusion loss parameter is a modified development of work by Reneau et al. (1967). The diffusion loss is a function of the divergence parameter (D) and the diffusion efficiency (E). The diffusion loss is mathematically described as:

$$\bar{\omega}_{Df} = -2.0(1-E)\left(\frac{C_{3,id} - C_2}{\rho_2 C_2} \right) \tag{3.79}$$

The divergence parameter is mathematically described as:

$$D = \frac{b_2 \left(\frac{A_3}{A_2} - 1 \right)}{L} \tag{3.80}$$

Diffusion losses are low if the divergence parameter is less then:

$$D_m = 0.4 \left(\frac{b_2}{L} \right)^{0.35} \tag{3.81}$$

The diffusion efficiency has a boundary condition that that is mathematically described as:

$$\begin{aligned} &E = 1;\ D \le 0 \\ &E = 1 - 0.2\left(D / D_m\right)^2;\ 0 < D < D_m \\ &E = 0.8\sqrt{D_m / D};\ D \ge D_m \end{aligned} \tag{3.82}$$

The actual total pressure is the difference of the ideal total pressure and the total pressure loss. The actual total pressure is used to calculate the other actual exit conditions of the vaneless diffuser using the velocity diagrams, total temperature relationship to calculate the static temperature, the total pressure relationship to calculate

the static pressure, the density, and the assumption that the total temperature is constant due to constant enthalpy. The actual exit conditions can be used to determine the component mean thermodynamic efficiency and power consumption parameters.

Vaned Diffuser

The non-dimensional loss parameter for the vaned diffuser is converted into a total pressure loss. The total pressure loss conversion can be mathematically described as (Aungier. 2000):

$$\Delta p_{t4} = (p_{t3} - p_{s3}) \sum_i \bar{\omega}_i \tag{3.83}$$

The loss parameters are calculated using an approach similar to that for the impeller and vaneless diffuser. The loss parameters are calculated using the inlet, throat, and isentropic exit conditions. The inlet conditions are equal to the actual exit conditions of the vaneless diffuser.

There are five non-dimensional vaned diffuser losses evaluated by Aungier (1990 and 2000). Mathematically, the non-dimensional losses are described in the following section. The loss that has the greatest effect on compressor efficiency/discharge pressure is the skin friction loss and is a function of the boundary layer approximation $\left(2\delta / D_H\right)$. The vaned diffuser skin friction is also a function of the friction coefficient $\left(c_f\right)$. The friction coefficient development is described in the impeller loss parameter section described earlier using equations 3.34 through 3.41. The vaned diffuser skin friction loss parameter and boundary layer approximation are mathematically described as (Aungier. 1990 and 2000):

$$\bar{\omega}_{SF} = 4c_f \left(\frac{C_{avg}}{C_3} \right)^2 \frac{L_B / D_H}{\left(2\delta / D_H\right)^{0.25}} \tag{3.84}$$

$$\frac{2\delta}{D_H} = \frac{5.142 c_f L_B}{D_H} \leq 1 \tag{3.85}$$

The incidence loss in the vaned diffuser also plays a large role in the pressure loss in the vaned diffuser. The incidence loss for the vaned diffuser has a boundary condition dependent on the absolute stall velocity C_{3S} described as (Aungier. 1990 and 2000):

$$C_{3S} = \frac{C_{m3}}{\sin \alpha_{3S}} \tag{3.86}$$

The incidence loss parameter is mathematically described as (Aungier. 1990 and 2000):

$$\bar{\omega}_{inc} = 0.8\left(\frac{C_3 - C_3^*}{C_3} \right)^2 ;\ C_3 \le C_{3S} \tag{3.87}$$

$$\bar{\omega}_{inc} = 0.8\left[\left(\left(\frac{C_3}{C_{3S}} \right)^2 - 1 \right) \frac{C_{Th}^2}{C_3^2} + \frac{C_{3S} - C_3^*}{C_{3S}^2} \right];\ C_3 > C_{3S} \tag{3.88}$$

The vaned diffuser incidence loss parameters are functions of the velocity at the optimum incidence angle $\left(C_3^*\right)$ that is mathematically described as (Aungier. 1990 and 2000):

$$\frac{C_{m3}}{C_3^*} = \sqrt{\sin\left(\beta_3\right)\sin\left(\alpha_{Th}\right)} \tag{3.89}$$

The loss due to choking for the vaned diffuser requires the calculation of a contraction ratio $\left(C_r\right)$ and a constraint condition $\left(X\right)$. Similar to the impeller the constraint condition must be greater than zero, otherwise the choke loss is zero. The choke loss and

constraint conditions are mathematically described as (Aungier. 1990 and 2000):

$$\bar{\omega}_{CH} = \frac{1}{2}\left(0.05X + X^7\right) \tag{3.90}$$

$$X = 11 - \frac{10 C_r A_{Th}}{A^*};\ \left(X > 0\right) \tag{3.91}$$

$$C_r = \sqrt{\frac{A_3 \sin\left(\theta_3\right)}{A_{Th}}} \tag{3.92}$$

The expansion loss, also known as the blockage loss in the vaned diffuser, is a function of the tip distortion factor (λ), which in turn is a function of tip blockage (B_4). The expansion loss is mathematically described in terms of the distortion factor and tip blockage term as (Aungier. 1990 and 2000):

$$\bar{\omega}_{\lambda} = \left[\frac{(\lambda - 1)C_{m4}}{C_4}\right]^2 \tag{3.93}$$

$$\lambda = \frac{1}{1 - B_4} \tag{3.94}$$

The tip blockage is a function dependent on the blade-to-blade width (w) and blockage correlations $(\bar{C}_R, K_1, K_2)$ which are mathematically described as (Aungier. 1990 and 2000):

$$B_4 = \frac{\left[K_1 + K_2\left(\bar{C}_R^2 - 1\right)\right]L_B}{w_4} \tag{3.95}$$

$$w = \frac{2\pi r \sin(\beta)}{Z} \tag{3.96}$$

$$\bar{C}_R = \frac{1}{2}\left[\frac{C_{m3}\sin(\beta_4)}{C_{m4}\sin(\beta_3)} + 1\right] \tag{3.97}$$

$$K_1 = 0.2\left[1 - \frac{1}{C_L C_\theta}\right] \tag{3.98}$$

$$K_2 = \frac{2\theta_C}{125 C_\theta}\left[1 - \frac{2\theta_C}{22 C_\theta}\right] \tag{3.99}$$

The blockage correlations depend on the diffuser divergence angle (θ_C), the mean streamline length (L), and the average blade-to-blade velocity difference (ΔC) which are

mathematically described as (Aungier. 1990 and 2000):

$$1 \le C_\theta \ge \frac{2\theta_C}{11} \tag{3.100}$$

$$1 \le C_L \ge 3L \tag{3.101}$$

$$2\theta_C = 2\tan^{-1}\left\{\frac{\left(w_4 - t_{b4}\right)\frac{b_4}{b_3} - w_3 + t_{b3}}{2L_B}\right\} \tag{3.102}$$

$$L = \frac{\Delta C}{C_3 - C_4} \tag{3.103}$$

$$\Delta C = 2\pi \frac{r_3 C_{U3} - r_4 C_{U4}}{Z L_B} \tag{3.104}$$

The final loss term that is applicable to the vaned diffuser is the wake mixing loss. The wake mixing loss functionally depends on the separation velocity in the vaned diffuser and is mathematically described as (Aungier. 1990 and 2000):

$$\bar{\omega}_{MIX} = \left[\frac{C_{m,wake} - C_{m,mix}}{C_3}\right]^2 \tag{3.105}$$

$$C_{m,wake} = \sqrt{C_{SEP}^2 - C_{U4}^2} \tag{3.106}$$

$$C_{m,mix} = \frac{A_4 C_{m4}}{2\pi r_4 b_4} \tag{3.107}$$

$$C_{SEP} = \frac{C_3}{1 + 2C_\theta} \ge C_4 \tag{3.108}$$

The actual total pressure loss is the difference of the isentropic total pressure and the total pressure loss. The actual vaned diffuser conditions are calculated using the actual total pressure, the assumption that the total temperature is constant, the velocity diagram, the compressible relationships for pressure and temperature, fluid density, and a flow angle deviation.

The actual exit flow angle of the vaned diffuser is calculated using a correlation of the deviation angle and incidence angle developed by Johnsen and Bullock (1965) and are mathematically described as:

$$\alpha_4 = \theta_4 - \delta^* - \frac{\partial \delta}{\partial i}\left(\theta_3 - \alpha_3\right) \tag{3.109}$$

$$\frac{\partial \delta}{\partial i} = \exp\left[\psi\left(\left(1.5 - \frac{\theta_3}{60^\circ}\right)^2 - 3.3\right)\right] \tag{3.110}$$

The vaned diffuser exit deviation angle $\left(\delta^*\right)$ is a correlation developed by Howell (1947). The deviation angle is a function of the blade angles $\left(\theta\right)$, maximum camber $\left(a/c\right)$, solidity $\left(\psi\right)$, and camber angle $\left(\Theta\right)$ which are mathematically described as (Howell. 1947):

$$\delta^* = \frac{\Theta\left[0.92\left(a/c\right)^2 + 0.02\left(90^\circ - \theta_4\right)\right]}{\sqrt{\psi} - 0.02\Theta} \tag{3.111}$$

$$a/c = \frac{\left[2 - \left(\bar{\theta} - \theta_3\right)/\left(\Theta\right)\right]}{3} \tag{3.112}$$

$$\psi = \frac{z\left(r_4 - r_3\right)}{2\pi r_3 \sin\left(\bar{\theta}\right)} \tag{3.113}$$

$$\Theta = \theta_4 - \theta_3 \tag{3.114}$$

The actual vaned diffuser exit conditions can be used to determine the component mean thermodynamic efficiency and power consumption parameters.

Volute

The volute is the final component of the centrifugal compressor. The non-dimensional loss parameter for the vaned diffuser is converted into a total pressure loss. The total pressure loss conversion can be mathematically described as (Aungier. 2000):

$$\Delta p_{t5} = (p_{t4} - p_{s4})\sum_i \bar{\omega}_i \tag{3.115}$$

The inlet conditions of the volute are equal to the exit conditions of the actual vaned diffuser. Similar to the previous components, the volute uses the approach of calculating the isentropic exit parameters. Aungier (2000) describes an improved upon one-dimensional volute analysis originally developed by Weber and Koronowski (1986). The volute has four non-dimensional losses mathematically described below. The meridional velocity loss equation is (Aungier. 2000):

$$\bar{\omega}_m = \left(\frac{C_{m4}}{C_4} \right)^2 \tag{3.116}$$

The tangential velocity loss has a volute sizing parameter (SP) boundary condition applied to it and is mathematically described as (Aungier. 2000):

$$\bar{\omega}_U = \frac{1}{2} \frac{r_4 C_{U4}^2}{r_5 C_4^2} \left[1 - \frac{1}{SP^2} \right]; \ (SP \geq 1) \tag{3.117}$$

$$\bar{\omega}_U = \frac{r_4 C_{U4}^2}{r_5 C_4^2} \left[1 - \frac{1}{SP} \right]^2; \ (SP < 1) \tag{3.118}$$

$$SP = \frac{r_4 C_{U4}}{r_5 C_5} \tag{3.119}$$

The skin friction loss is a function of the mean stream line path length (L) through the volute, the hydraulic diameter (D_H), and the friction coefficient (c_f) that was previously described in the impeller section using equations 3.34 through 3.41. The skin friction coefficient is mathematically described as (Aungier. 2000):

$$\bar{\omega}_{SF} = 4 c_f \left(\frac{C_5}{C_4} \right)^2 \frac{L}{D_H} \tag{3.120}$$

$$L = \frac{\pi (r_4 + r_5)}{2} \tag{3.121}$$

$$D_H = \sqrt{\frac{4 A_5}{\pi}} \tag{3.122}$$

The exit cone loss is mathematically described as (Aungier. 2000):

$$\bar{\omega}_{EC} = \left[\frac{C_5 - C_6}{C_4} \right]^2 \tag{3.123}$$

The actual total pressure loss is the difference of the isentropic total pressure and the total pressure loss. The actual volute conditions are calculated using the actual total pressure, the assumption that the total temperature is constant, velocity diagram, compressible relationships for pressure and temperature, density, and a radius to tangential velocity correlation developed from the conservation of mass. The basic cone diffuser correlation is mathematically described as:

$$C_{U4} r_4 = C_{U5} r_5 \tag{3.124}$$

The actual volute exit conditions can be used to determine the component mean thermodynamic efficiency and power consumption parameters.

Mathematical Description Summary

Once the component mean thermodynamic efficiency, power consumption, and loss parameters have been mathematically described the compressor model as a whole has been described mathematically. The component parameters required the calculation of inlet and exit conditions. All the information was calculated from the known ambient conditions, geometry, and assumptions. With all the information for each component available, an analysis of the loss parameters can show what has the greatest effect on the compressor system and what effect a change in known conditions has on the loss parameters. The change in known conditions can be used to develop a higher thermodynamically efficient turbocharger compressor. The equations that described the compressor have been determined and a process to solve the equations is developed in the next chapter.

CHAPTER 4 - Solving the mathematical description for the compressor

Now that the compressor has been mathematically described, a method is needed to simultaneously solve the extensive set of derived equations. Solving the equations from Chapter 3 by hand is possible, but with today's technologies it seems more useful to develop a computer model that can solve the set of equations. The method of using a computer model to solve the set of equations is outlined in this chapter.

The derived equations from Chapter 3 were solved using a FORTRAN program called TuCMS. TuCMS stands for Turbocharger Component Matching System. Figure 4.1 illustrates the flow diagram of the compressor side for the TuCMS FORTRAN program. The flow diagram in Figure 4.1 shows the method of coupling the components of the compressor together into one system. The term "station" was defined in Chapter 3 and was used to identify the interface between two adjacent components. These stations can be thought of as "virtual measurement points." The program inputs are the ambient temperature and pressure, rotational speed, fluid mass flow rate, and component geometry. The geometry input into the system is the component diameters, component passage heights, component flow areas, impeller and vaned diffuser blade angles, impeller and vaned diffuser blade thicknesses, impeller and vaned diffuser blade quantities, impeller and shroud clearances, and material surface roughness.

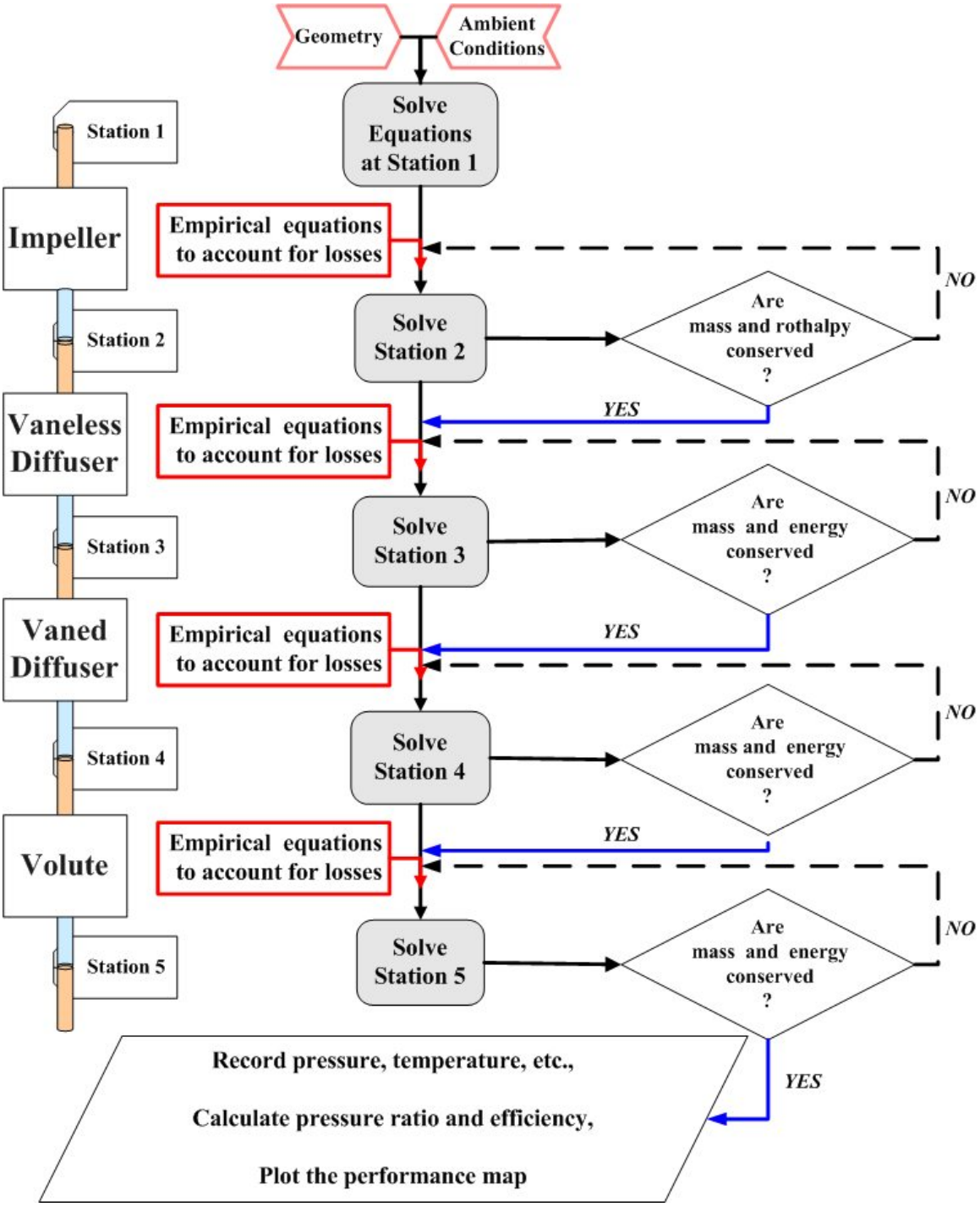

Figure 4.1 Compressor modeling technique flow diagram (Sengupta, et al. 2007)

Station 1, as shown in Figure 4.1, was evaluated using the compressor geometry and ambient conditions. The stations downstream are subsequently evaluated using upstream results and appropriate equations connecting the inlet and exit of each component. For the impeller, rothalpy (defined as the difference between the total

enthalpy and angular momentum) remained constant across the component due to its rotating frame of reference, while the enthalpy remained constant across stationary components (Aungier. 2000).

The general procedure is to first calculate the isentropic (ideal) conditions through the impeller. Second, the isentropic conditions are used to quantify the various losses that occur in the impeller. The last step is to transform the impeller exit conditions into meaningful parameters that can be compared to measured data. The impeller exit conditions are then used as inlet conditions to the vaneless diffuser. The vaneless diffuser leads to the vaned diffuser, which then leads to the compressor volute.

The impeller is the only part of the compressor that rotates, therefore all the calculations must be done in a rotating frame of reference also known as the relative frame of reference. Figure 4.2 shows the flow chart of the component model for the compressor impeller. The flow diagram first reads in the input information from a file or graphical user interface and proceeds to the first subroutine to solve the inlet conditions of the impeller using the equations from Chapter 3. The set of equations calculates the velocities, Mach numbers, temperatures, pressures, and fluid density. This information is saved and passed to the "losses" subroutine and "impeller throat" subroutine where again the velocities, Mach numbers, temperatures, pressures, and density are calculated. The throat information is saved and passed to the "losses" subroutine and the "isentropic exit" subroutine. The "isentropic exit" subroutine uses the information from the previous subroutines to calculate the velocities, Mach numbers, temperatures, pressures, and density. The information is saved and passed to the losses subroutine and actual exit subroutine. In the "losses" subroutine all the information needed is now available and the losses from Chapter 3 are calculated and converted to a pressure loss. The pressure loss is passed to the "actual exit" subroutine were the actual conditions are calculated for the impeller exit. The actual exit conditions are now passed to the vaneless diffuser inlet were a similar set of subroutines is used to calculate that components conditions. The process continues until all the component parameters have been calculated.

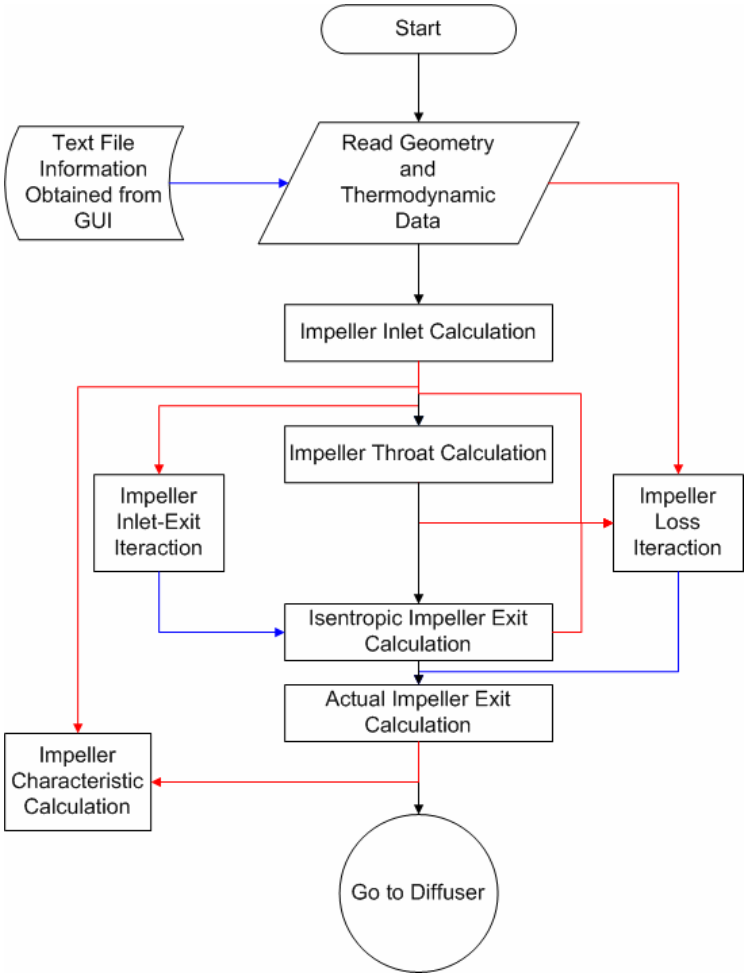

Figure 4.2 Impeller modeling flow chart (Sengupta, et al. 2007)

The subroutines that calculate the inlet, throat, isentropic, and actual conditions use an International Mathematical and Statistical Library (IMSL) function. The TuCMS program utilizes the Newton-Raphson method algorithm from the library to solve the non-linear equations simultaneously. The idea of the Newton-Raphson method is as follows: start with an initial guess that is reasonably close to the true root using trial and error, then the function is approximated by its tangent line (which can be computed using calculus), and compute the *x*-intercept of this tangent line (which is computed with algebra). This *x*-intercept will typically be a better approximation to the function's root than the original guess, and the method can be iterated until the solutions converge.

The IMSL function used in the TuCMS program is the *DNEQNF* function that is used to solve a system of non-linear equations using a modified Powell hybrid algorithm

and a finite-difference approximation to the Jacobian. The TuCMS program calls the *DNEQNF* function as:

CALL *DNEQNF* (*FCN*, *ERRREL, N*, *ITMAX*, *XGUESS, X*, *FNORM*)

The *DNEQNF* function has the arguments described as:

- *FCN* – User supplied subroutine to evaluate the system of equations to be solved. The usage is CALL *FCN* (*X*, *F*, *N*)
    - *X* – The point at which the functions are evaluated. (Input)
    - *F* – The computed function values at the point *X*. (Output)
    - *N* – Length of *X* and *N*. (Input)
- *ERRREL* – Stopping criterion. The root is accepted if the relative error between two successive approximations to this root is less than *ERRREL*. *ERRREL* = 0.000000001. (Input)
- *N* – The number of equations to be solved and the number of unknowns. (Input)
- *ITMAX* – The maximum allowable number of iterations. *ITMAX* = 200. (Input)
- *XGUESS* – A vector of length *N*. *XGUESS* contains the initial estimate of the root. (Input)
- *X* – A vector of length *N*. *X* contains the best estimate of the root found by *DNEQNF*. (Output)
- *FNORM* – A scalar that has the value $F(1)^2 + ... + F\left(N\right)^2$ at the point *X*. *FNORM* is the deviation for the system of equations. (Output)

CHAPTER 5 - Results and analysis

With the compressor model complete using the method described in Chapter 4, the program is ready to analyze a centrifugal compressor. Experimental data collected by the researchers at the NGML on the VGT turbocharger, developed from an ET-18 compressor, was used to compare with the TuCMS modeled data of the same ET-18 compressor.

Experimental Procedure

The VGT was experimentally tested at different vane positions and rotational speeds. The VGT was tested at the NGML facility using the Turbocharger Test and Research Facility (TTRF), which is a closed loop turbocharger test cell. The VGT was first experimentally tested at a vane position labeled "neutral" which is a vane angle of 66° from the radial axis. The VGT was then experimentally tested at a vane position labeled "10° counter clockwise (CCW)" which is a vane angle of 76° from the radial axis. The VGT was further experimentally tested at a vane position labeled "10° clockwise (CW)" which is a vane angle of 56° from the radial axis. The three vane positions were experimentally tested at three rotational speeds, 10,000 rpm, 13,000 rpm, and 14,500 rpm. The research team collected the experimental data by locating three data points on a constant speed line for each particular scenario for example, the neutral vane position at 13,000 rpm). The three points collected by the research team were choke, surge, and a halfway point between the choke and surge. The research team collected the three points for the turbocharger first by adjusting the turbocharger to the rotational speed that was being tested. To achieve the mass flow rate through the compressor a load valve at the compressor discharge was adjusted. The first data point of the constant rotational speed line collected was the choking condition. No load, or a very small load, was applied to the compressor to achieve choking conditions and the research team recorded the data point. The test cell is a closed loop system and is limited by the flow rate. The test cell is unable to produce a high enough flow rate for the compressor to actually reach a choking condition. The highest flow rate can only be achieved by applying no load, or

a very small load, on the load valve. Therefore, the experimental data is unable to fully investigate the actual choking condition. Thus, the experimental data only shows a representation of the actual choking condition. The research team proceeded to locate the surge condition at the constant rotational speed by increasing the compressor load until surge occurs; then this data point was then collected. The research team then reduced the compressor load to a condition halfway between the choking and surge conditions to record a third point on the speed line. The above process was repeated for each scenario.

The uncertainty of the test cell for experimental data was calculated to be plus or minus five percent with respect to the air mass flow rate and plus or minus a tenth of a percent with respect to the pressure ratio. The uncertainty is represented in Figure 5.1 through Figure 5.3 using error bars.

Model Procedure

The VGT compressor geometry was measured by hand and inputted to the TuCMS program. The measured VGT compressor geometry is located in Appendix A. The experimental test data collected from the TTRF contained inlet ambient conditions (temperature and pressure) and operating conditions (rotational speed and air mass flow rate). The experimental inlet ambient and operating conditions were used as input information for the TuCMS program. The TuCMS program was run for each of the experimental scenarios and the results collected. The TuCMS program was run at a constant rotational speed and varying air mass flow rate until a maximum pressure ratio was achieved which was the determinate for surge conditions. In the program, the air mass flow rate was increased incrementally until a choking condition was reached. The choking condition typically occured in the vaned diffuser throat when the flow angle reached a negative value. At a negative throat flow angle the program was unable to calculate a solution because the program reached an iteration maximum which means the solution is no longer converging. Reaching the maximum iteration terminates the program. The mass flow rate was decreased until the program was able to complete all the calculations and at this point the choking data is recorded. The speed line produced by the TuCMS program and the experimental data collected by the research team at NGML are compared in the next section.

Model and Experimental Performance Comparison

In Figure 5.1 the experimental data and the TuCMS model data for the neutral vane position and different rotational speeds are compared. The comparison of the model and experimental data in Figure 5.1 is shown as a compressor performance map.

The modeled data for the compressor shows the compressor operating at higher mass flow rates than the experimental data. The experimental data for stonewall does not represent an actual stonewall condition for the VGT compressor because the test cell used to collect the experimental data has a limited mass flow rate due the closed loop design of the test cell. The experimental stonewall condition would occur at an increased mass flow rate that could match closer to the modeled data. The modeled stonewall condition for the compressor is a stonewall condition. Surge for the experimental data is an actual surge condition for the VGT compressor. Surge for the compressor was achieved experimentally because during operation, the compressor started to vibrate at an unstable rate which means the compressor was in surge. The modeled data for surge was assumed to occur at the highest pressure ratio or when the slope of the speed line being collected became negative. The assumption of the change in slope for the modeled surge condition is conservative and surge could occur at a reduced mass flow rate that matches closer to the experimental data.

Qualitatively, the model is a good representation of the experimental data because of similar trends. A possible reason, but one that was beyond the scope of this work, that the modeled data is different from the experimental data is the potential sensitivity of the calculated results to the compressor geometry input information. Another possible reason is that the empirical loss models developed in Chapter 4 are general models and need to be specifically tuned to the VGT compressor.

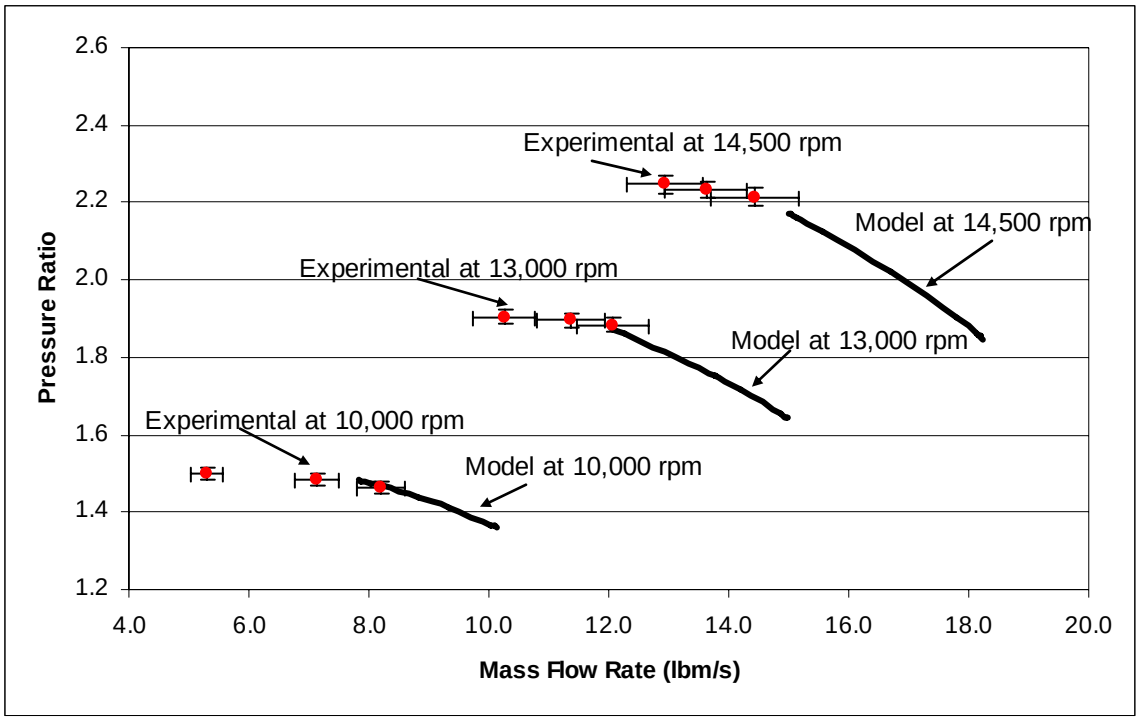

Figure 5.1 Performance map – neutral vane position

In Figure 5.2 the experimental data and the TuCMS model data for the 10° counter clockwise (CCW) vane position and different rotational speeds are compared. The model data at the 10° counter clockwise represents a compressor map that has an increased operating range compared to the experimental data. The modeled data shows the compressor operating at a greater pressure ratio then the experimental data, but the operating mass flow range encompasses the experimental data. Again, the compressor geometry input into the program is a possible factor to the modeled data and experimental data not being a closer match. The general empirical loss models can also be tuned to the VGT compressor. Qualitatively the modeled data is a good representation of the experimental data.

As the vane position changes from neutral to 10° CCW, the compressor's experimental and modeled speed lines shift to decreased mass flow rates for the different rotational speeds. The compressor's mass flow rate for the experimental data decreases by about two lbm/s for the 13,000 rpm and 14,500 rpm rotational speeds. The compressor's mass flow rate for the experimental data does not significantly change at 10,000 rpm. The compressor's pressure ratio for the experimental data at 14,500 rpm shows a decrease of about one tenth. The compressor's pressure ratio for the

experimental data at 10,000 rpm and 13,000 rpm rotational speed line appears to not have a significant change with a 10° increase in vane angle from the neutral position. The compressor's mass flow rate for the modeled data decreased but more significantly then the experimental data. The decrease in compressor mass flow rate for the modeled data shows a similar trend as the experimental data with a 10° increase in vane angle from the neutral vane position. The compressor's mass flow rate for the modeled data at 10,000 rpm decreases about four lbm/s but increases in range of operation about two lbm/s. The compressor's pressure ratio for the modeled data at 10,000 rpm increases about a tenth. The compressor's mass flow rate for the modeled data at 13,000 rpm decreases about six lbm/s but also increases in range of operation about two lbm/s. The compressor's pressure ratio for the modeled data at 13,000 rpm increases about two tenths. The compressor's mass flow rate for the modeled data at 14,500 rpm decreases about eight lbm/s but increases in range of operation about three lbm/s. The compressor's pressure ratio for the modeled data at 14,500 rpm is increased by about two tenths. The changes in the modeled data can more easily be seen when investigating the utility of the VGT concept in Figure 5.4 through Figure 5.6.

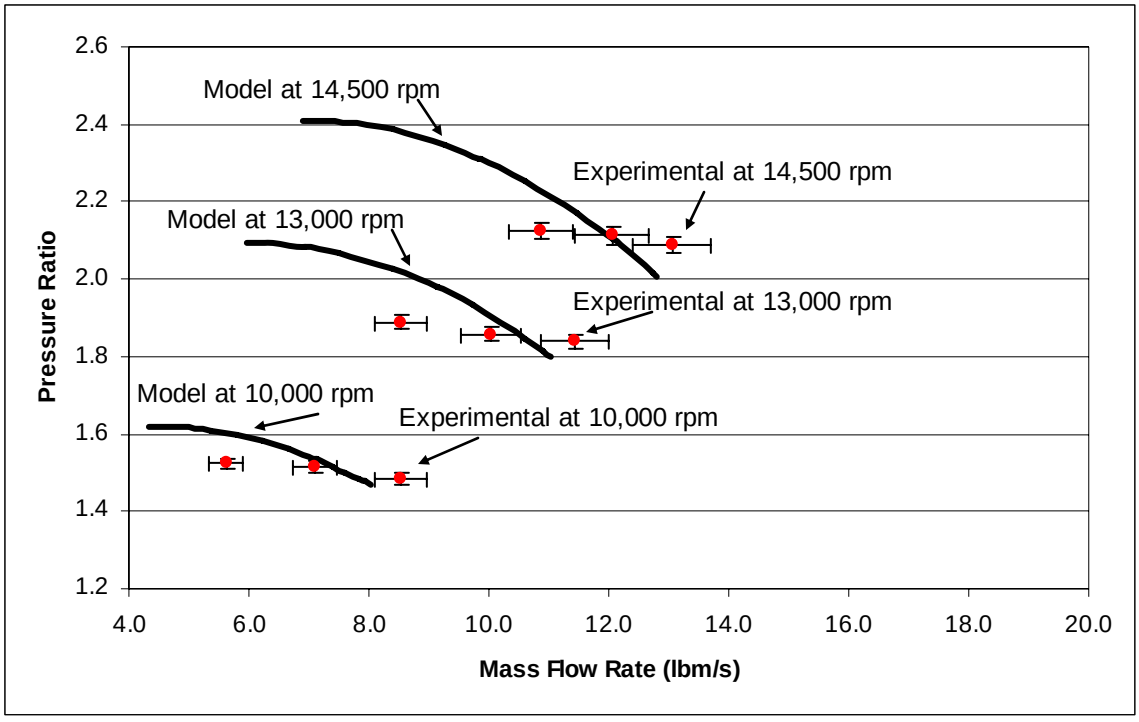

Figure 5.2 Performance map – 10° CCW vane position

In Figure 5.3 the experimental data and the TuCMS model data for the 10° clockwise (CW) vane position and different rotational speeds are compared. The experimental data and modeled data comparison may seem to be extremely different in Figure 5.3, but when comparing the overall trend of the data the modeled data is a good representation of the experimental data. Comparing the trends of the speed lines at 14,500 rpm the experimental and modeled data both show the compressor's mass flow rate operating range is limited. As the rotational speed is decreased the compressor's operating range increases in both the experimental and modeled data. As the rotational speed is decreased from 14,500 rpm to 13,000 rpm the compressor's mass flow rate operating range increases about one lbm/s experimentally and increases about one and a half lbm/s modeled. As the rotational speed is decreased from 13,000 rpm to 10,000 rpm the compressor's mass flow rate operating range increases about one lbm/s for the experimental data and remains unchanged for the modeled data. The modeled data again shows the compressor operating at a higher mass flow rate then the experimental data. The reason for this shift in mass flow rate operation is possibly due to the compressor geometry input into the TuCMS program and the general empirical loss model developed in Chapter 4 are not specifically tuned to the VGT compressor. From Figure 5.3 the 10° clockwise vane position is likely a poor vane position for the operation of the VGT compressor. Figure 5.3 shows the compressor's experimental data and modeled data having limited operating ranges compared to the previous described vane positions. The modeled data also shows the compressor having low pressure ratios and high mass flow rates at the 10° CW vane position.

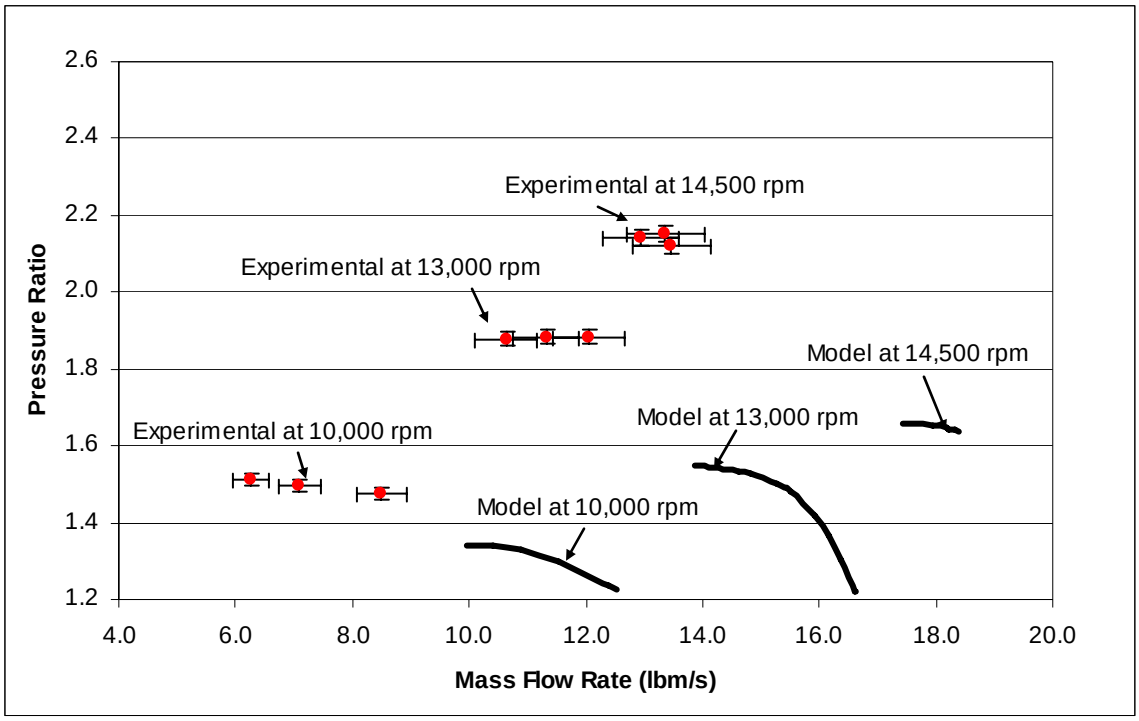

Figure 5.3 Performance map – 10° CW vane position

Investigating the Utility of the VGT Concept

The performance maps of each vane position were compared above. Comparing the characteristics of the VGT at constant speed lines and varying blade position is the next point of interest. The comparison of different vane angles at constant speed lines is of importance because the affects of the VGT are more easily seen.

In Figure 5.4 the TuCMS model data for a constant rotational speed of 10,000 rpm and varying blade positions are compared. The modeled data shows that as the vane position is changed the pressure ratio and operating range is changed. From Figure 5.4 the VGT concept can be seen in that the operating range has significantly increased as the vane position is changed. When modeled the VGT is performing how it was conceptually designed. For example, from the modeled data if the VGT was operating at a neutral vane position and the load is significantly increased thus causing a reduction in mass flow rate the diffuser vanes can be turned 10° counter clockwise moving and expanding the compressor's operating range to a lower mass flow rate thus avoiding compressor surge. Another example is if the compressor is asked to push more mass

flow, the vane position can be adjusted to 10° clockwise and the compressor avoids choking.

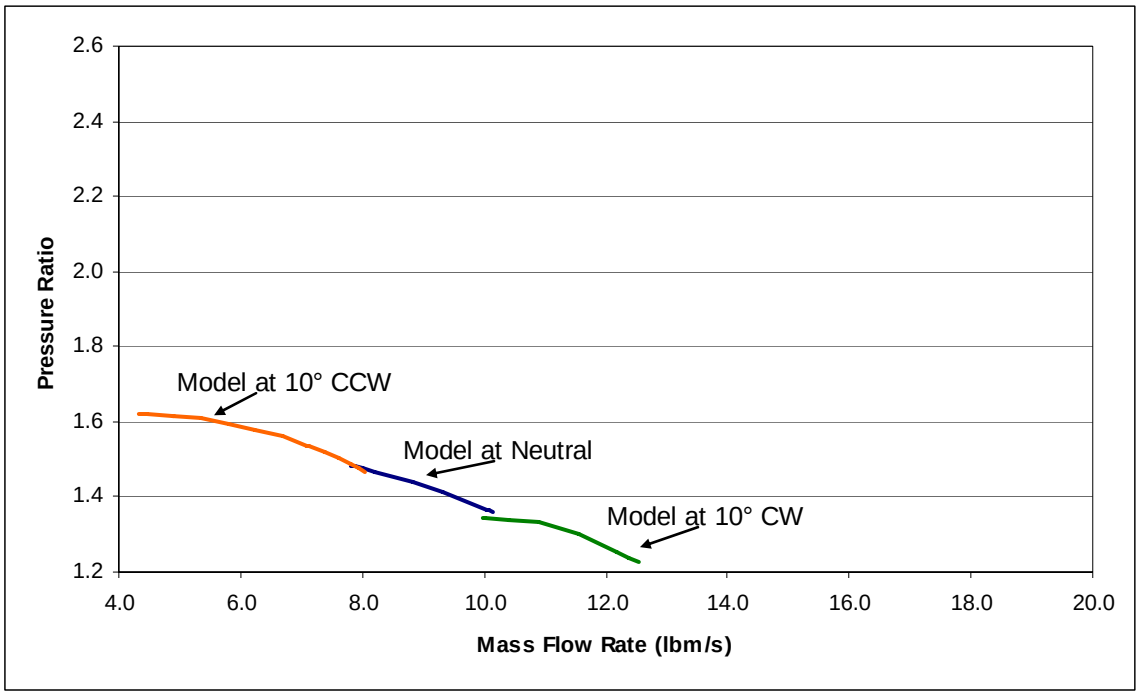

Figure 5.4 Vane position comparison for constant rotational speed of 10,000 rpm

In Figure 5.5 the TuCMS model data for a constant rotational speed of 13,000 rpm and varying blade positions are compared. The modeled data also shows the VGT concept of an increased operating range.

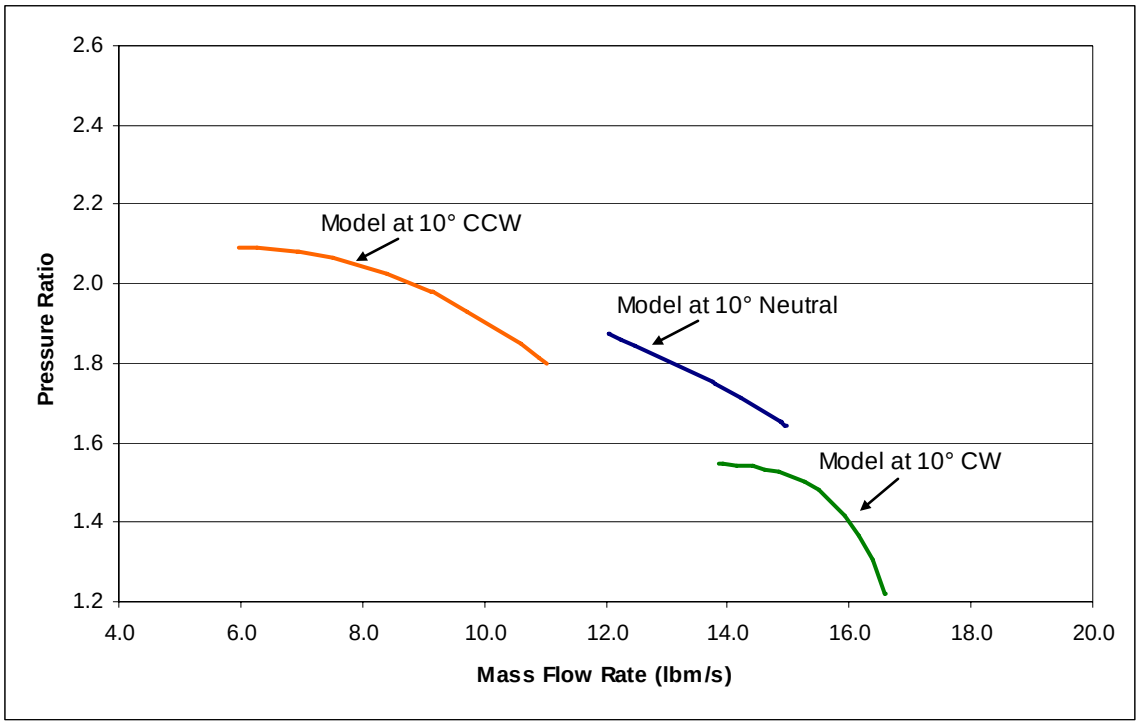

Figure 5.5 Vane position comparison for constant rotational speed of 13,000 rpm

In Figure 5.6 the TuCMS model data for a constant rotational speed of 14,500 rpm and varying blade positions are compared. The modeled data shows the VGT concept of an increased operating range is still evident.

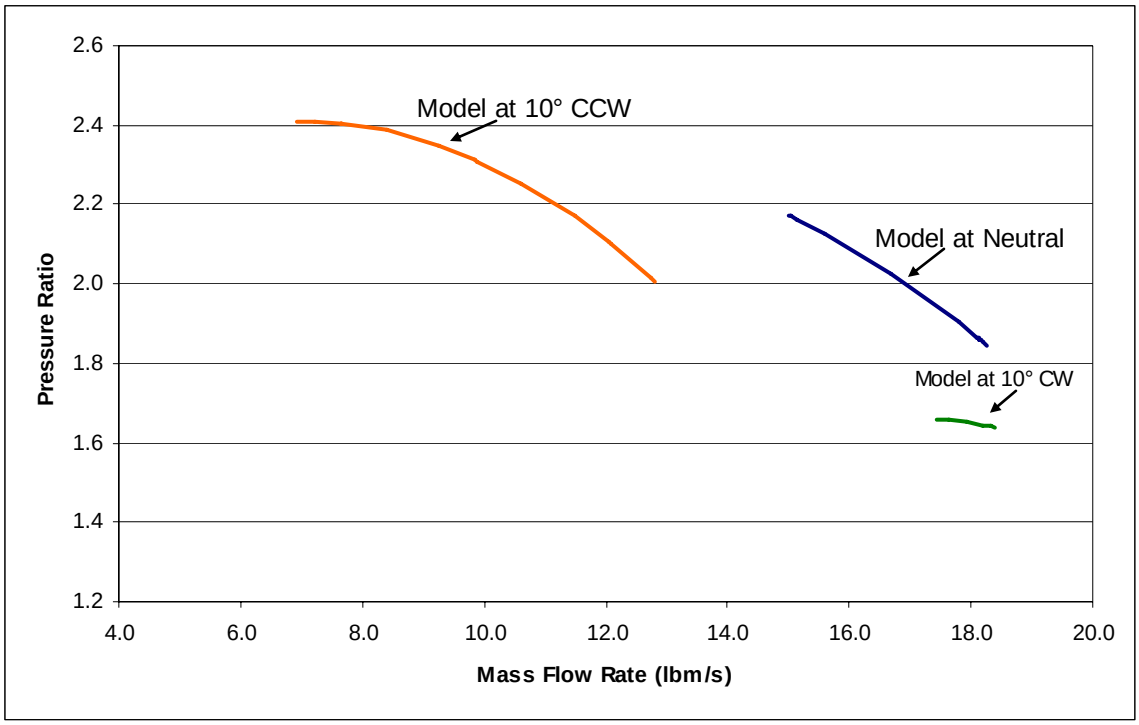

Figure 5.6 Vane position comparison for constant rotational speed of 14,500 rpm

From Figures 5.4 through 5.6 the VGT concept of an increased operating range is very noticeable.

Loss Analysis

The next modeling interest is the analysis of the losses seen throughout the compressor. The losses shown in Figure 5.7 through Figure 5.9 all come from the model. The model shows the losses are lower than those that must exist in the actual turbocharger. Future work should be to investigate ways to decrease the compressor losses in the actual turbocharger to achieve the much wider operating capability suggested by the model in the above investigations.

The losses at the different diffuser vane positions showed changes. However, the losses had similar characteristics as the rotational speed was increased at each vane position. Therefore, the loss comparisons of each vane position are compared for a rotational speed of 13,000 rpm.

In Figures 5.7 and 5.8 the TuCMS model data for losses at a neutral vane position and rotational speed of 13,000 rpm are compared. The losses are split between two figures because the impeller skin friction loss, represented in Figure 5.7, has the greatest

affect on the pressure loss. The loss affect is large enough that if all the losses were plotted on the same graph the details of the other losses would not be as obvious. Figure 5.8 shows other losses in the compressor. Only the losses that have the greatest affect (categorized as being greater than a tenth of a psi pressure loss) have been graphed for comparison. Each loss graphed shows the actual pressure loss for the model. The sum of the losses would be the total pressure loss.

The loss analysis is associated with the empirical loss models developed in Chapter 3.

- The impeller skin friction loss has the greatest affect on the pressure loss and increases with mass flow rate because it is a function of Reynolds number. The Reynolds number is a function of absolute velocity. The absolute velocity increases as mass flow rate increases.
- The volute meridional velocity head loss increases as the mass flow rate increases because the loss is a function of the volute inlet absolute meridional velocity, which increases with an increase in mass flow rate.
- The vaned diffuser incidence loss approaches zero and then increases. The shape of the vaned diffuser loss is parabolic and the minimum indicates the optimum mass flow rate to minimize the incidence loss in the vaned diffuser.
- The impeller incidence loss continuously decreases because as the mass flow rate increases the ratio of the absolute meridional velocity over the relative velocity increases in equation 3.28 of Chapter 3. The ratio is being subtracted from one and as the ratio increases with the mass flow rate the impeller incidence loss decreases. The incidence loss characteristic is as the mass flow rate increases the incidence angle decreases. The incidence angle is the difference between the relative flow angle and the blade angle. The relative flow angle is a trigonometric function of the relative velocity and absolute meridional velocity vectors.
- The vaned diffuser and vaneless diffuser skin friction losses remain fairly constant. Due to a short passage length that does not allow the skin friction in these components to increase significantly as the mass flow rate increases.

Other empirical losses that were described in Chapter 4 increase as the mass flow rate increases.

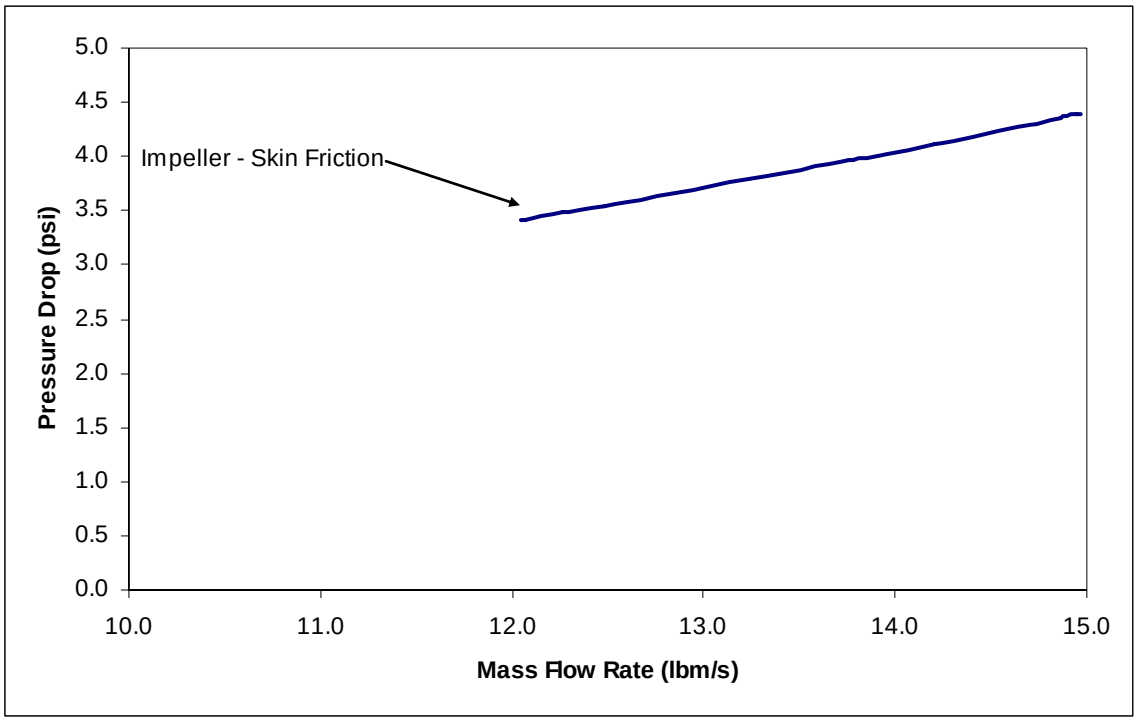

Figure 5.7 Impeller skin friction loss for a neutral vane position at 13,000 rpm

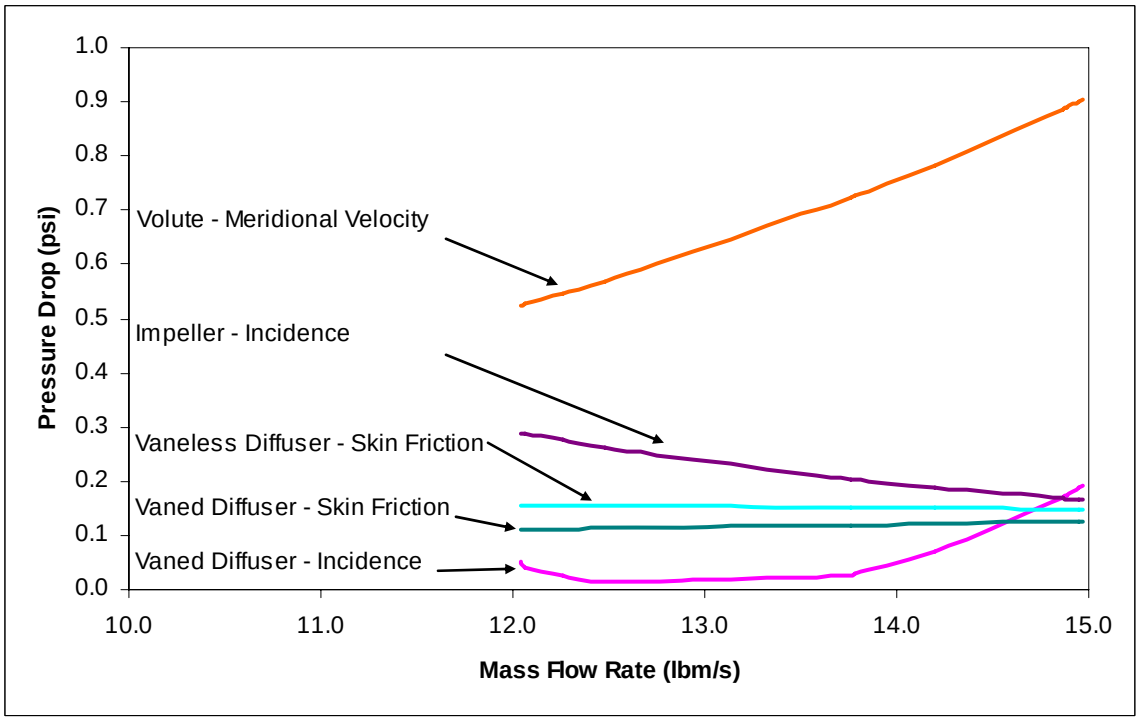

Figure 5.8 Comparison of other losses for a neutral vane position at 13,000 rpm

In Figures 5.9 and 5.10 the TuCMS model data for losses at a 10° counter clockwise vane position and rotational speed of 13,000 rpm are compared. The losses are again represented by two graphs so the details of the not-so-significant losses can be viewed without the impeller skin friction skewing the plotted data. Figure 5.9 is the impeller skin friction, which is similar to that shown for the neutral position. The impeller skin friction loss increases with the mass flow rate due to the Reynolds number increasing with the increase in mass flow rate. Figure 5.10 is the comparison of the other losses that affect the compressor at the 10° counter clockwise vane position. Again, the losses in Figure 5.10 are the losses that have a greater pressure loss then a tenth of a psi.

- The volute meridional velocity head loss increases with mass flow rate due to the increase in meridional velocity at the volute inlet.
- The vaned diffuser incidence loss has a more pronounced parabolic curve due to the flow angle and blade angles not matching as well until the mass flow rate is increased to an optimum point. The vaned diffuser incidence loss is quite significant because it shows the limit of operating the VGT. The vaned diffuser incidence loss also shows that slight off-design operation can be a disaster. At the optimum mass flow rate the flow angle is changed with the increase in absolute velocity which is directly proportional to the mass flow rate.
- The impeller incidence loss has a greater affect in the 10° counter clockwise because the mass flow rate is lower than the mass flow rate at the neutral vane position. The ratio of the absolute meridional velocity over the relative velocity decreases for lower mass flow rates causing the incidence angle to increase, thus a greater impeller incidence loss.
- The vaneless diffuser and vaned diffuser skin friction losses remain fairly constant. The passage length for the two components is short enough to not allow the skin friction to increase with the mass flow rate.
- At the 10° counter clockwise vane position a vaned diffuser wake-mixing loss has an accountable affect. The vaned diffuser wake-mixing loss occurs at low mass flow rates because the flow rate is low enough not to wash out the

mixing. As the mass flow rate increases the wake-mixing loss approaches zero because now the mass flow rate is high enough to not allow the mixing of the wakes to take place.

Other losses described in Chapter 3 increase as the mass flow rate increases but do not have as great of an impact on the compressor pressure loss.

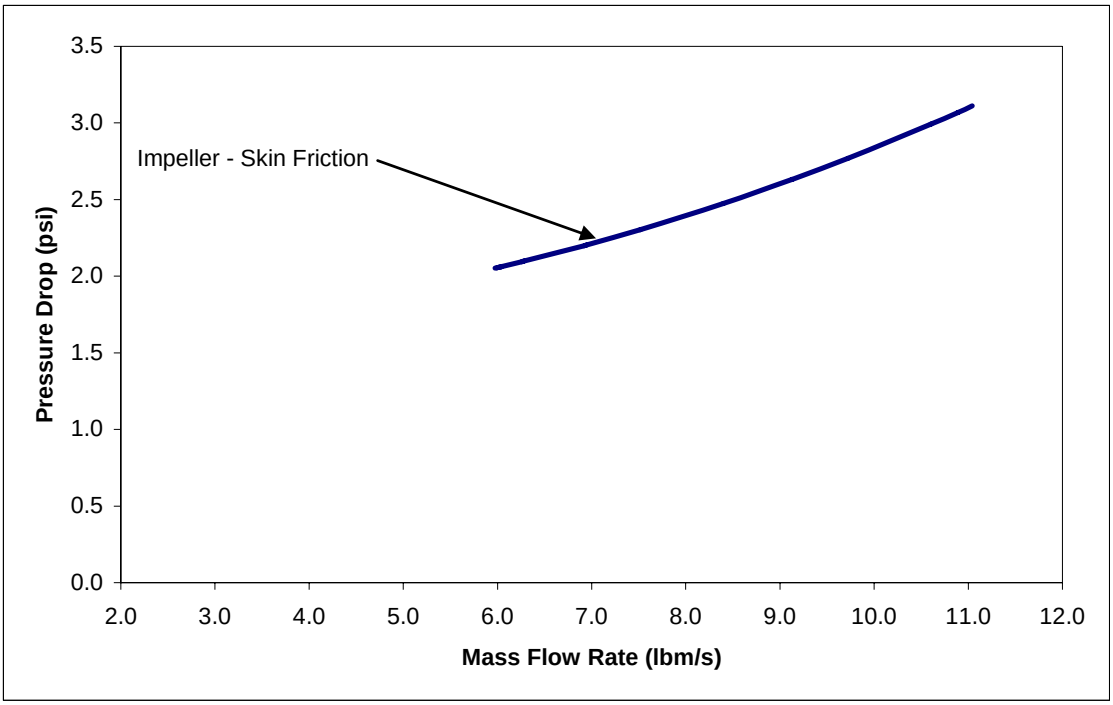

Figure 5.9 Impeller skin friction loss for a 10° CCW vane position at 13,000 rpm

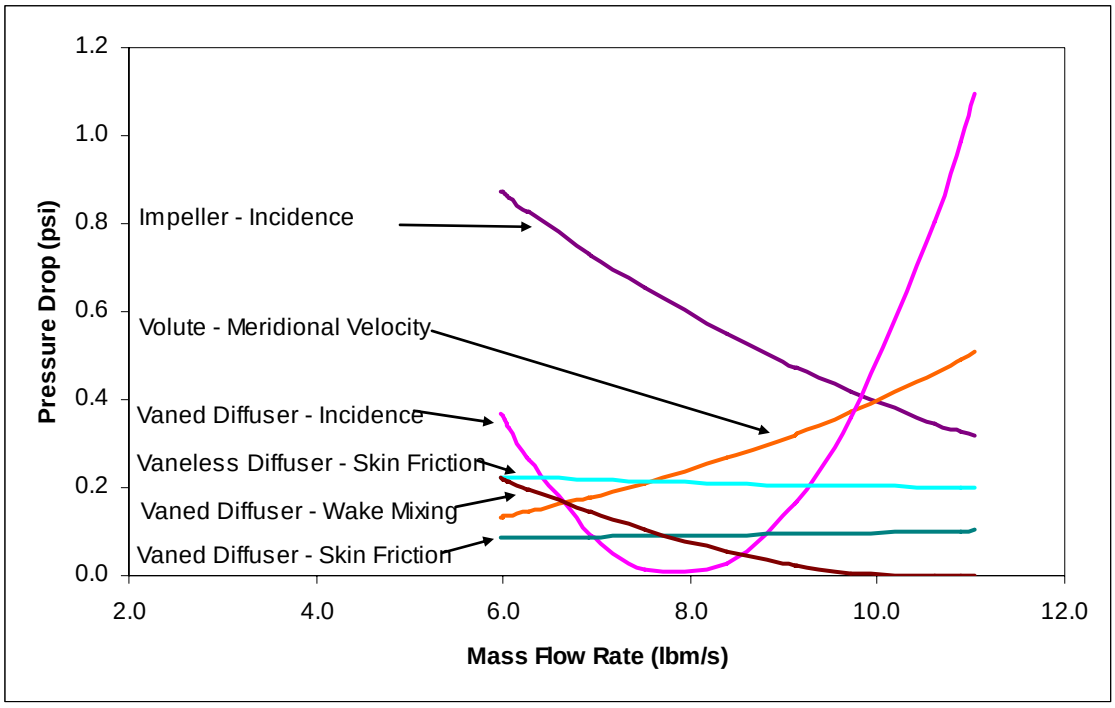

Figure 5.10 Comparison of other losses for a 10° CCW vane position at 13,000 rpm

In Figures 5.11 and 5.12 the TuCMS model data for losses at a 10° clockwise vane position and rotational speed of 13,000 rpm are compared. Two graphs were used to compare the losses so that the impeller skin friction and vaned diffuser choke losses would not skew the details to the other losses that do not have as great of an impact on the compressor pressure loss for the 10° clockwise vane position. Figure 5.11 is the graph that compares the impeller skin friction and vaned diffuser choking loss.

- The impeller skin friction loss, which similar in the other vane positions, is continuously increasing because the impeller skin friction is a function of Reynolds number.
- The vaned diffuser choking loss exponentially increases as the mass flow rate increases. The exponential increase is due to the variable (X) in the choking loss equation 3.90 of Chapter 3 being raised to the power of seven. The variable (X) in equation 3.91 of Chapter 3 is a function of the vane inlet area and vane blade angles both of which are constants. The variable (X) is also a function of the sonic area which is a function of inlet area, throat area, inlet Mach number and throat Mach number. Mach number is directly proportional

to the absolute velocity which is directly proportional to the to mass flow rate using equation 3.15 of Chapter 3. The choking loss is evident at the 10° clockwise vane position because the mass flow rate for this vane position to operate is higher compared to the mass flow rate at the neutral position.

Figure 5.12 is the graph of the other losses that have a greater pressure loss than a tenth of a psi.

- The vaned diffuser incidence loss has a large affect at the low flow rate and approaches zero at the higher flow rates. This is caused by the air flow angle for the vaned diffuser inlet not matching very closely with the vane blade angle. The incidence angle (difference between the flow angle and blade angle) decreases as the mass flow rate increases causing the vaned diffuser incidence angle to decrease. The vaned diffuser is still slightly parabolic and the optimum point has shifted to the near choke limit.
- The volute meridional velocity head loss increases as the mass flow increases due to an increase in the meridional velocity at the inlet of the volute.
- The impeller incidence at this high flow rate has a smaller affect on the pressure loss and decreases as the mass flow rate increases. This occurs do to similar reasons discussed for the impeller incidence loss at the previous vane positions.
- The vaned diffuser and vaneless diffuser skin friction losses remain fairly constant due to the reason discussed in the previous vane positions.

The other losses described in Chapter 3 increase as the mass flow rate increases but at a less significant impact to the compressor pressure loss. The losses provide another reason the 10° clockwise vane position is not a good operating range for the VGT compressor. At the high mass flow rates that the 10° clockwise vane position must operate, this vane position introduces losses such as the choking loss and changes the other losses such as the vaned diffuser incidence loss significantly shifting it, both of which affect the compressor pressure loss.

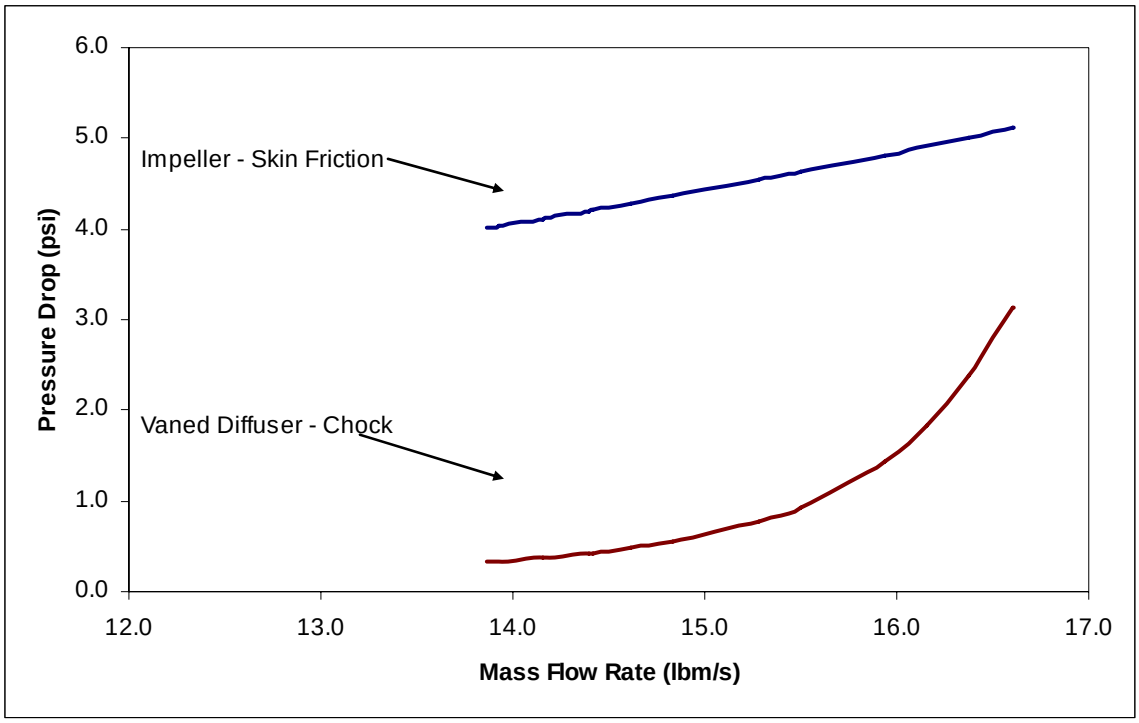

Figure 5.11 Comparison of high losses for a 10° CW vane position at 13,000 rpm

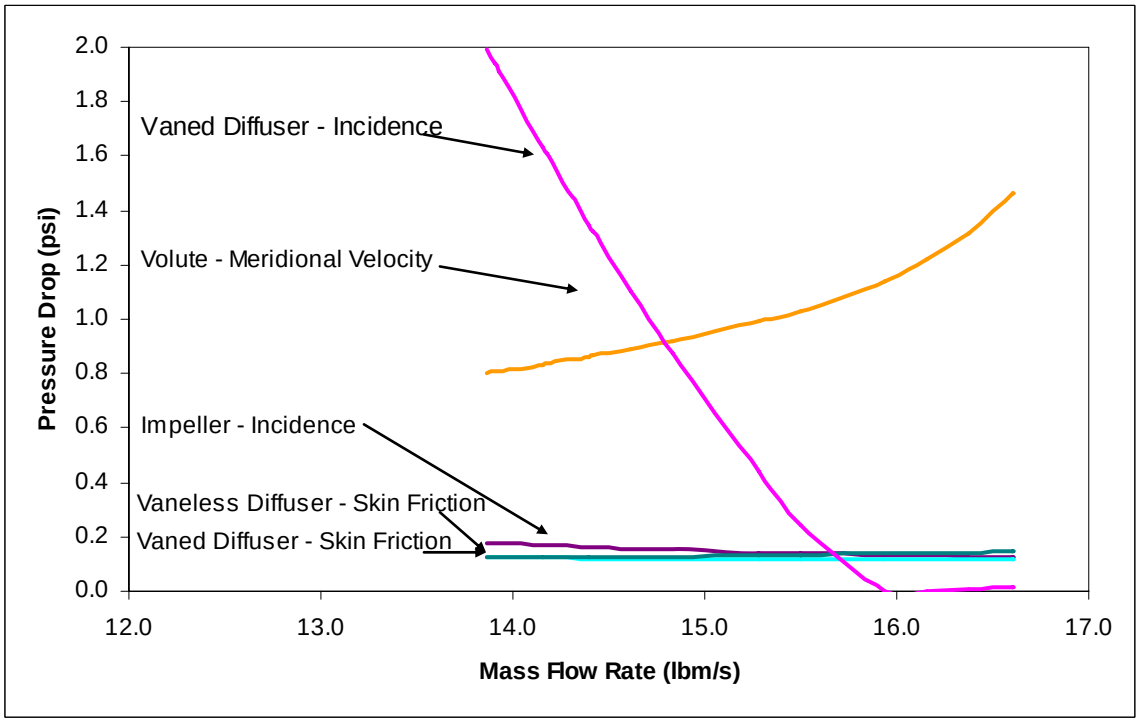

Figure 5.12 Comparison of other losses for a 10° CW vane position at 13,000 rpm

CHAPTER 6 - Conclusion

This chapter outlines the achieved objectives of this thesis, conclusions drawn from the objectives, and suggests future work towards the continued development of this research.

- A one-dimensional model simulation based on first engineering principles was developed to analyze a centrifugal compressor. The model individually analyzes each compressor component using information from the previous component. The model was developed using multiple loss models developed from the literature instead of a lump sum loss or slip factor.
- The model developed is robust and can analyze a magnitude of different compressor geometries. The ability to analyze different geometries has been demonstrated by the model data for different diffuser vane positions of the VGT.
- The TuCMS model was used to develop a performance analysis on the VGT turbocharger. The TuCMS results qualitatively represented the experimental data for the VGT well.
    - As the diffuser vane position was changed the experimental and modeled data shifted right for the clockwise vane position and left for the counter clockwise vane position compared to the neutral vane position.
    - As the diffuser vane position was changed the experimental and modeled data operating ranges had similar trends. The 10° counter clockwise position demonstrated an increase in operating range and the 10° clockwise vane position demonstrated a decrease in operating range compared to the neutral vane position.

  The TuCMS program supports the VGT concept of an increased operating range.
- The losses can be graphed to see what is having the greatest effect on the compressors overall pressure loss.

- The experimental and model comparison investigation and the loss analysis investigation both show the vane position of 10° clockwise is not a good position to operate the VGT compressor. The experimental and model comparison showed the mass flow operating range to be limited as the compressor rotational speed is increased. The loss analysis for the 10° clockwise position introduced a choke loss due to the very high mass flow rate operating values once again showing the vane position is not a good position to operate the VGT compressor.
- The loss analysis investigation for the vaned diffuser incidence loss shows that it limits operation of the VGT. The vaned diffuser incidence loss can be used to estimate the optimal vane angle of a given mass flow rate in the VGT compressor. The vaned diffuser incidence loss also shows that slight off-design can cause unsuitable compressor operation.

The future work in this research would be to:

- Identify why the VGT ET-18 compressor did not fit the experimental data by:
  - Tuning the loss models; and
  - Performing a sensitivity test on the compressor geometry. The compressor geometry is very important to the analysis. The compressor geometry was measured from the actual compressor using hand tools (ruler, calipers, and protractor) instead of computer aided drafting tools that can be used to get the highest precision measurements. Development of a better way to collect geometry measurements would assist in the tuning of the model.
- Explore the diffuser vane position sensitivity; and
- Couple the compressor model with a turbine model to create a complete model for the turbocharger component matching system.

Overall the compressor model developed during the research of this thesis is a first step to developing a one-dimensional turbocharger component matching system. With further development, the compressor model could be used to search a data base of component geometry and compile a compressor that precisely matched to deliver a precise amount of air to the engine and assist in the reduction of emissions.

References

Aungier, R.H., 1988, "A Performance Analysis for the Vaneless Comonents of Centrifugal Compressors," Flows in Non-Rotating Turbomachinery Components, ASME, Vol. 69, 35-43.

Aungier, R.H., 1990, "Aerodynamic Performance Analysis of Vaned Diffusers," Fluid Machinery Components, ASME, Vol. 101, 27-44.

Aungier, R.H., 1993, "Mean Streamline Aerodynamic Performance Analysis of Centrifugal Compressors," Proceedings Rotating Machinery Conference and Exposition (ROCON'93), Vol. I. (Also in Transactions ASME, Journal of Turbomachinery, July 1995, 360-366.)

Aungier, R.H., 2000, Centrifugal Compressors a Strategy for Aerodynamic Design and Analysis, ASME Press, New York.

Baines, N.C., 2005, Fundamentals of Turbocharging, Concepts NREC, Vermont.

Bathie, W.W., 1996, Fundamental of Gas Turbines, 2nd Ed., John Wiley & Sons, Inc., New York.

Benedict, R.P., Carlucci, N.A., and Swetz, S.D., 1966, "Flow Losses in Abrupt Enlargements and Contractions," Transactions ASME, Journal of Engineering for Power, Jan., 73-81.

Boyce, M.P., 2003, Centrifugal Compressors a Basic Guide, PennWell Corporation, Oklahoma.

Chapman, K.S., Keshavarz, A., and Honegger, U., 2007, "Variable Geometry Turbocharger," Pipeline Research Council International, Inc. Report No. PR-266-9920, Virginia.

Cohen, H., Rogers, G.F.C., and Saravanamuttoo, H.I.H., 1972, Gas Turbine Theory, 3rd Ed. Longman Scientific and Technical, John Wiley & Sons, New York.

Engine Logics Inc., http://www.enginelogics.com/cmaps.html, Houston, TX.

Heywood, J.B., 1988, Internal Combustion Engine Fundamentals, McGraw-Hill, Inc. New York.

Howell, A.R., 1947, “Development of the British Gas Turbine Unit,” Lecture: Fluid Dynamic of Axial Compressors, ASME Reprint, New York.

Japikse, D., 1996, Centrifugal Compressor Design and Performance, Concepts ETI, Inc., Vermont.

Johnsen, I.A. and Bullock, R.O., eds., 1965, “Aerodynamic Design of Axial Flow Compressors,” NASA SP-36, Fig. 177.

Lieblein, S. (1959). “Loss and Stall Analysis of Compressor Cascades,” ASME Transactions, Journal of Basic Engineering, Sept., 387-400.

MAN B&W Diesel AG, 2008, http://www.manbw.com/files/news/filesof6685/TCA.pdf, Germany.

Mattingly, J.D., 1996, Elements of Gas Turbine Propulsion, McGraw-Hill, Inc., New York.

Nunn, R.H., 1989, Intermediate Fluid Mechanics, Hemisphere Publishing Corporation, New York.

Reneau, L., Johnston, J., and Kline, S., 1967, “Performance and Design of Straight Tow-Dimensional Diffusers,” Transactions ASME, Journal of Basic Engineering, Mar., 141-150.

Sengupta, J., Erickson, C., Chapman, K.S., and Kesavarz, A. (2007). “Turbocharger Component Matching System Development” Proceedings of the Internal Combustion Engine Division Fall Technical Conference Paper No. ICEF2007-1767, South Carolina.

Weber, C.R. and Koronowski, M.E., 1986, “Meanline Performance Predictions of Volutes in Centrifugal Compressors,” Paper No. 86-GT-216, ASME, New York.

Appendix A - VGT Measurements

Table A.1 represents the operating conditions for one of the scenarios described in Chapter 5.

Table A. 1 Operating Conditions for VGT compressor at 13,000 rpm

	English Units	Metric Units
Inlet Static Temperature (°F and K)	51.2500	283.8444
Inlet Static Pressure (psi and Pa)	14.0000	96526.5980
Rotational Speed (rpm)	13000.0000	13000.0000
Mass Flow Rate (lbm/s and kg/s)	11.3800	5.1619

Table A.2 is the impeller geometry measurements. Stared measurements are input into the TuCMS model.

Table A. 2 Impeller geometry

	English Units	Metric Units
Inlet Hub Diameter (in/m)	4.3540	0.1106
Inlet Shroud Diameter (in/m)	11.3010	0.2870
Inlet Blade Thickness (in/m)	0.1468	0.0037
* Inlet Area (in^2/m^2)	75.7279	0.0489
* Inlet Root Mean Radius (in/m)	4.2818	0.1088
Inlet Hub Blade Angle (°) w/r to axis	51.4000	51.4000
Inlet Shroud Blade Angle (°) w/r to axis	37.5000	37.5000
* Inlet Root Mean Blade Angle (°)	44.9901	44.9901
* Inlet Cone Angle (°) w/r to axis	21.2132	21.2132
* Throat Area (in^2/m^2)	50.8250	0.0328
Throat Hub Blade Angle (°)	47.5000	47.5000
Throat Shroud Blade Angle (°)	50.5000	50.5000
* Throat Root Mean Blade Angle (°)	49.0230	49.0230
Discharge Diameter (in/m)	18.0000	0.4572
* Discharge Radius (in/m)	9.0000	0.2286
* Discharge Blade Height (in/m)	0.9380	0.0238
* Discharge Blade Thickness (in/m)	0.2538	0.0064
* Discharge Area ($in^2/m^{2)}$	48.5194	0.0313
* Discharge Blade Angle (°) w/r to radial	26.2377	26.2377
* Discharge Cone Angle (°) w/r to radial	75.1665	75.1665
* Number of Vanes	19.0000	19.0000
* Shroud Clearance (in/m)	0.0175	0.0004
* Mean Blade Passage Length (in/m)	7.1875	0.1826
* Surface Roughness (in/m)	0.00013	0.000003

Table A.3 is the vaneless diffuser geometry for the varying blade angles of the VGT. Stared measurements are input into the TuCMS model.

Table A. 3 Vaneless Diffuser Geometry

	10° CCW	Neutral	10° CW
	English/Metric	English/Metric	English/Metric
Inlet Diameter (in/m)	18.0000 / 0.4572	18.0000 / 0.4572	18.0000 / 0.4572
* Inlet Radius (in/m)	9.0000 / 0.2286	9.0000 / 0.2286	9.0000 / 0.2286
* Inlet Passage Height (in/m)	0.9380 / 0.0238	0.9380 / 0.0238	0.9380 / 0.0238
* Inlet Area (in^2/m^2)	53.0427 / 0.0342	53.0427 / 0.0342	53.0427 / 0.0342
Discharge Diameter (in/m)	21.6200 / 0.5491	21.2980 / 0.5410	20.9960 / 0.5333
* Discharge Radius (in/m)	10.8100 / 0.2746	10.6490 / 0.2705	10.4980 / 0.2666
* Discharge Passage Height (in/m)	0.9750 / 0.0248	0.9750 / 0.0248	0.9750 / 0.0248
* Discharge Area (in^2/m^2)	66.2232 / 0.0427	65.2369 / 0.0421	64.3119 / 0.0415

Table A.4 is the vaned diffuser geometry for varying vane positions of the VGT. Stared measurements are input into the TuCMS model.

Table A. 4Vaned Diffuser Geometry

	10° CCW	Neutral	10° CW
	English/Metric	English/Metric	English/Metric
Inlet Diameter (in/m)	21.6200 / 0.5491	21.2980 / 0.5410	20.9960 / 0.5333
* Inlet Radius (in/m)	10.8100 / 0.2746	10.6490 / 0.2705	10.4980 / 0.2666
* Inlet Passage Height (in/m)	0.9750 / 0.0248	0.9750 / 0.0248	0.9750 / 0.0248
* Inlet Blade Thickness (in/m)	0.1000 / 0.0025	0.1000 / 0.0025	0.1000 / 0.0025
* Inlet Area (in^2/m^2)	64.7607 / 0.0418	63.7744 / 0.0411	62.8494 / 0.0405
* Inlet Blade Angle (°) w/r to tangent	8.8500	19.0790	29.4710
* Throat width (in/m)	1.5600 / 0.0396	2.1510 / 0.0546	2.6700 / 0.0678
* Throat Area (in^2/m^2)	22.8150 / 0.0147	31.4550 / 0.0203	39.0450 / 0.0252
Discharge Diameter (in/m)	24.0700 / 0.6114	24.9280 / 0.6332	25.6980 / 0.6527
* Discharge Radius (in/m)	12.0350 / 0.3057	12.4640 / 0.3166	12.8490 / 0.3264
* Discharge Passage Height (in/m)	0.9750 / 0.0248	0.9750 / 0.0248	0.9750 / 0.0248
* Discharge Blade thickness (in/m)	0.1000 / 0.0025	0.1000 / 0.0025	0.1000 / 0.0025
* Discharge Area (in^2/m^2)	72.2652 / 0.0466	74.8933 / 0.0483	77.2518 / 0.0498
* Exit Blade Angle	47.5210	46.2720	44.7840

(°) w/r to tangent			
* Number of Vanes	15.0000	15.0000	15.0000
* Blade Length (in/m)	3.9000 / 0.0991	3.9000 / 0.0991	3.9000 / 0.0991

Table A.5 is the volute geometry for the VGT at varying vane positions. Stared measurements are input into the TuCMS model.

Table A. 5 Volute Geometry

	10° CCW	Neutral	10° CW
	English/Metric	English/Metric	English/Metric
Inlet Diameter (in/m)	24.0700 / 0.6114	24.9280 / 0.6332	25.6980 / 0.6527
* Inlet Radius (in/m)	12.0350 / 0.3057	12.4640 / 0.3166	12.8490 / 0.3264
* Inlet Passage Height (in/m)	0.9750 / 0.0248	0.9750 / 0.0248	0.9750 / 0.0248
* Inlet Area (in^2/m^2)	73.7277 / 0.0476	76.3558 / 0.0493	78.7143 / 0.0508
Discharge Diameter (in/m)	30.0000 / 0.7620	30.0000 / 0.7620	30.0000 / 0.7620
* Discharge Radius (in/m)	15.0000 / 0.3810	15.0000 / 0.3810	15.0000 / 0.3810
* Discharge Area (in^2/m^2)	104.7700 / 0.0676	104.7700 / 0.0676	104.7700 / 0.0676

Table A. 6 Exit Cone Geomtry

	English Units	Metric Units
Inlet Diameter (in/m)	14.0000	0.3556
* Inlet Area (in^2/m^2)	104.7700	0.0676
Discharge Diameter (in/m)	15.0000	0.3810
* Discharge Area (in^2/m^2)	153.9380	0.0993